HEALTH AND MEDICINE

# Tumor-specific delivery of clickable inhibitor for PD-L1 degradation and mitigating resistance of radioimmunotherapy

**Bo Hou[1,2,3]†, Jiayi Ye[2,4]†, Lujia Huang[2,4]†, Wenhao Cheng[2], Fangmin Chen[2,4], Huiling Zhou[1,2], Jiaxing Pan[2], Jing Gao[2], Yi Lai[2], Yujun Zhao[5], Wei Huang[6], Haijun Yu[2,3,4], Zhiai Xu[1]***



**Achieving selective and durable inhibition of programmed death ligand 1 (PD-L1) in tumors for T cell activation remains a major challenge in immune checkpoint blockade therapy. We herein presented a set of clickable inhibitors for spatially confined PD-L1 degradation and radioimmunotherapy of cancer. Using metabolic glycan engineering click bioorthogonal chemistry, PD-L1 expressed on tumor cell membranes was labeled with highly active azide groups. This enables covalently binding of the clickable inhibitor with PD-L1 and subsequent PD-L1 degradation. A pH-activatable nanoparticle responding to extracellular acidic pH of tumor was subsequently used to deliver the clickable PD-L1 inhibitor into extracellular tumor microenvironment for depleting PD-L1 on the surface of tumor cell and macrophage membranes in vivo. We further demonstrated that a combination of the clickable PD-L1 inhibitor with radiotherapy (RT) eradicated the established tumor by inhibiting RT–up-regulated PD-L1 in the tumor tissue. Therefore, selective PD-L1 blockade in tumors via the clickable PD-L1 inhibitor offers a versatile approach to promote cancer immunotherapy.**

## INTRODUCTION

Cancer immunotherapy leverages the patient's immune system to eradicate tumors (*1*, *2*). The advances of immune checkpoint blockade (ICB) therapy had spurred the development of a range of antibodies and small-molecule inhibitors for cancer immunotherapy over the past decade. Among the immune checkpoints exploited so far, programmed death ligand 1 (PD-L1), expressed on the surface of tumor cell membrane, critically induces inhibitory signals by interacting with programmed cell death 1 (PD-1) on the surface of T cells (*3*–*5*). This PD-1/PD-L1 interaction suppresses tumor-specific T cell responses, functioning as a tumor immune evasion mechanism by inhibiting T lymphocyte proliferation and cytokine secretion, culminating in the exhaustion and apoptosis of tumor-infiltrating cytotoxic T lymphocytes (CTLs) (*6*–*8*). With the robust and strong antitumor immune responses provoked by ICB therapy, several therapeutic antibodies that block the PD-1/PD-L1 interaction have been approved for clinical treatment of the hematologic and solid tumors (*9*, *10*). However, the antibody-based PD-L1 inhibitors suffer from severe immune-related adverse events (irAEs) in clinics due to their on-target but off-tumor binding with PD-L1 protein expressed on normal tissues (*11*). Furthermore, the therapeutic performance of anti–PD-L1 antibodies (αPD-L1) is compromised by limited penetration into the central region of the solid tumors. To address these challenges, small molecular counterparts of αPD-L1 were designed for blocking PD-L1/PD-1 interaction (*12*). These small-molecule PD-L1 inhibitors display potent advantage of a shorter blood clearance halftime than αPD-L1, which may benefit for dose modifications to minimize the irAEs and improve the benefit/risk ratio. Unfortunately, clinical translation of the small-molecule PD-L1 inhibitors is hampered by high administration dose and transient PD-L1 blockade effect due to their reversable binding with PD-L1 target and off-tumor distribution. Compared to the conventional small-molecule inhibitors, covalent inhibitors have been exploited for stable binding of the protein of targets via formation of covalent bond. The covalent inhibitors display enhanced binding affinity and potency, a prolonged action duration that surpasses the pharmacokinetics of the drug, an improved therapeutic index by reducing the dosage and frequency of administration, and the potential to suppress refractory targets (*13*, *14*). However, a practical strategy for covalent binding of the small-molecule inhibitor to PD-L1 protein in solid tumors, featuring efficient chemical reactivity and high specificity, remains to be developed.

Metabolic glycan labeling using unnatural sugars has emerged as a robust strategy for labeling cell membrane glycoproteins with the azide groups. These chemical tags, expressed on the surface of cell membrane, are extensively used for targeted delivery of the cargoes by effective chemical methods, like click chemistry between azide and dibenzocyclooctyne (DBCO) groups (*15*–*17*). In particular, the bioorthogonal click chemistry between azide and DBCO group can facilitate covalent attachment of the small-molecule inhibitors to PD-L1 glycoprotein, thus enabling selective PD-L1 degradation on the surface of cell membrane. To exploit the pathological cues of solid tumors for site-specific therapeutic delivery and precise therapy, stimuli-responsive nanoparticles responding to the endogenous or exogenous signals have been used for spatially tunable delivery and sequential release of the therapeutics. This approach has demonstrated notable improvement in treatment efficacy and reduced off-target effects (*18*, *19*). Specifically, tumor anaerobic glycolysis induces an extracellular acidic microenvironment ($pH_e$ of 6.5 to 6.8), has been exploited as a broad hallmark of tumors to trigger intratumoral activation of the acid-liable nanovectors (*20*–*22*).

[1]School of Chemistry and Molecular Engineering, East China Normal University, Shanghai 200241, China. [2]State Key Laboratory of Chemical Biology and Center of Pharmaceutics, Shanghai Institute of Materia Medica, Chinese Academy of Sciences, Shanghai 201203, China. [3]Yantai Key Laboratory of Nanomedicine & Advanced Preparations, Yantai Institute of Materia Medica, Shandong 264000, China. [4]University of Chinese Academy of Sciences, Beijing 100049, China. [5]State Key Laboratory of Drug Research and Small-Molecule Drug Research Center, Shanghai Institute of Materia Medica, Chinese Academy of Sciences, Shanghai 201203, China. [6]Center for Biotherapeutics Discovery Research, Shanghai Institute of Materia Medica, Chinese Academy of Sciences, Shanghai 201203, China.
*Corresponding author. Email: zaxu@chem.ecnu.edu.cn
†These authors contributed equally to this work.

In this study, we presented a biorthogonal click strategy for tumor-specific PD-L1 inhibition and boosting antitumor immunity. This strategy involves efficient PD-L1 blockade via covalent binding of the small-molecule inhibitors to PD-L1 on the surface of tumor cell membrane via click reaction. Through metabolic glycan labeling, highly reactive azide groups on the surface of tumor cell membrane can react with the DBCO-modified PD-L1 inhibitor D5B (Fig. 1A). To accomplish tumor-targeted PD-L1 blockade, the outperformed D5B was screened out and systemically delivered with a $pH_e$-responsive diblock copolymer PCP or PCPGd. D5B-loaded $pH_e$-activatable nanoparticles were further labeled with near-infrared fluorescence (NIRF) probes (namely, PCP@D5B) or magnetic resonance imaging (MRI) tracers (termed as PCPGd@D5B) for imaging-guided cancer radiotherapy (RT) (Fig. 1B). Upon intravenous injection, the PCP@D5B or PCPGd@D5B nanoparticles were activated in tumor extracellular microenvironment to release D5B, which undergo covalent binding with azide-labeled PD-L1 on the surface of tumor cell membrane, resulting in tumor-specific PD-L1 degradation (Fig. 1C). A combination of tumor-specific PD-L1 degradation on the membrane surface of tumor cells and tumor-associated macrophages (TAMs) and RT-induced immunogenic cell death (ICD) of tumor cells efficiently reversed the immunosuppressive tumor microenvironment (ITM) for inhibiting tumor growth. This combinatory therapy strategy also generated long-term immunological memory for inhibiting the abscopal tumor and preventing lung metastasis of 4T1 breast tumor (Fig. 1D).

## RESULTS

### The clickable inhibitors degraded PD-L1 on the surface of tumor cell membrane

PD-L1 expressed on the surface of tumor cell membrane is heavily glycosylated (*23*–*25*), which can be readily labeled with azide group on the nonreducing termini of glycan chains via azide-modified unnatural sugars, thus facilitating covalent binding of the clickable inhibitors with PD-L1 via a bioorthogonal click reaction. To evaluate the efficiency of PD-L1 inhibition with the clickable PD-L1 inhibitors, we first synthesized the tetra-acetylated *N*-azidoacetylmannosamine ($Ac_4$ManAz) and a library of DBCO-conjugated BMS-1 [termed as D1B, D3B, and D5B, respectively, according to the length of oligo(ethylene glycol) (OEG) spacer] (Fig. 2A and figs. S1 to S6). The small-molecule PD-L1 inhibitor BMS-1 was selected as the parental inhibitor due to its ability to bind the hydrophobic domain of the PD-L1 homodimer for inducing PD-L1 dimerization, internalization, and degradation in the lysosomal vesicles (*26*–*28*). The parental BMS-1 and DnB inhibitors displayed good biocompatibility in 4T1 breast and B16-F10 melanoma tumor cells in vitro (fig. S7, A to E).

To demonstrate click chemistry–enabled covalent binding of the small-molecule inhibitor with PD-L1 protein, a clickable fluorescein isothiocyanate (FITC) dye was synthesized by conjugating DBCO with FITC (namely, DBCO-FITC). 4T1 tumor cells were then incubated with $Ac_4$ManAz for 3 days and treated with DBCO-FITC for 24 hours. Confocal laser scanning microscopy (CLSM) and flow cytometry analysis revealed that $Ac_4$ManAz treatment notably increased the FITC fluorescence signal on the surface of cell membrane compared to the control group (fig. S7F), validating successful azide labeling of tumor cells.

We next investigated the PD-L1 degradation efficiency of the clickable PD-L1 inhibitors in azide-labeled 4T1 and B16-F10 tumor cells in vitro. Flow cytometry examination revealed that the parental BMS-1 and the clickable inhibitors all reduced PD-L1 abundance on the surface of tumor cell membrane in a dose-dependent manner. D5B outperformed BMS-1, D1B, and D3B for PD-L1 degradation in both 4T1 and B16-F10 tumor cells (Fig. 2, B and C, and fig. S7, G and H). For instance, the half-maximal PD-L1 degradation concentration [median effect concentration ($EC_{50}$)] values of D5B were determined to 5.4 and 6.2 μM in wild-type 4T1 and B16-F10 tumor cells, which was ~21.5- and 16.7-fold more efficient than the parental BMS-1 molecular, respectively (table S1). This superior PD-L1 degradation performance of D5B was attributed to the elongated length of the $OEG_5$ spacer to allow stable binding of BMS-1 with the hydrophobic domain of PD-L1 dimer on the surface of tumor cell membrane (Fig. 2D).

To confirm covalent binding–dependent PD-L1 degradation profile of D5B, tumor cells were treated with either BMS-1 or D5B, with or without azide labeling. Notably, without azide labeling of tumor cells, D5B displayed comparable PD-L1 degradation efficacy as BMS-1 in both kinds of tumor cells. In contrast to tumor cells without azide labeling, only D5B treatment of azide-labeled tumor cells expressively reduced PD-L1 abundance on the membrane surface (Fig. 2, E and F, and fig. S7, I and J), verifying covalent binding of D5B to PD-L1 via a click reaction between the DBCO and azide groups is crucial for effective PD-L1 degradation in vitro (Fig. 2G). D5B markedly reduced PD-L1 abundance on the surface of a broad spectrum of azide-labeled human and murine tumor cells, including MBA-MD-231 human breast cancer cells, HN30 human head and neck cancer cells, Panc02 murine pancreatic cancer cells, CT26/MC38 murine colorectal cancer cells, and A549 human non–small cell lung cancer cells. In contrast, free BMS-1 marginally affected PD-L1 abundance on the membrane surface of all these cell types (Fig. 2H and fig. S7K). These results suggested that the clickable PD-L1 inhibitor represents a robust and generalizable strategy for reducing PD-L1 abundance on the surface of tumor cells membrane, showcasing its potential for broad application in cancer immunotherapy.

### The clickable PD-L1 inhibitor mitigated immune tolerance by inhibiting IFN-γ–inducible PD-L1 up-regulation in tumor cells in vitro

It has been identified that interferon-γ (IFN-γ) secreted by tumor-infiltrating T cells up-regulates PD-L1 on the surface of tumor cells to exhaust CTLs and induce immune tolerance (Fig. 3A) (*29*, *30*). For instance, treatment of 4T1 and B16-F10 tumor cells with IFN-γ (12.5 ng/ml) remarkedly induced PD-L1 up-regulation, as validated by flow cytometry and Western blot analysis (fig. S8, A to C). To evaluate whether the clickable PD-L1 inhibitors could abolish IFN-γ–induced PD-L1 up-regulation and thereby mitigate the acquired immune resistance, PD-L1 inhibition was performed with the DnB library in both IFN-γ–pretreated 4T1 and B16-F10 tumor cells following azide labeling. As expected, flow cytometry examination displayed that D5B surpassed BMS-1, D1B, and D3B in terms of the PD-L1 inhibition efficacy in vitro (Fig. 3, B and C, and fig. S8, D and E). In particular, the $EC_{50}$ values of D5B decreased to 1.3 and 3.3 μM in IFN-γ–pretreated 4T1 and B16-F10 tumor cells, which were 44.3- and 9.8-fold lower than free BMS-1, respectively (table S1). Western blot and CLSM examinations further validated that D5B markedly reduced PD-L1 abundance on the surface of both 4T1 and B16-F10 tumor cell membrane in a dose-dependent manner, while BMS-1 negligibly reduced PD-L1 abundance (Fig. 3, D to F).

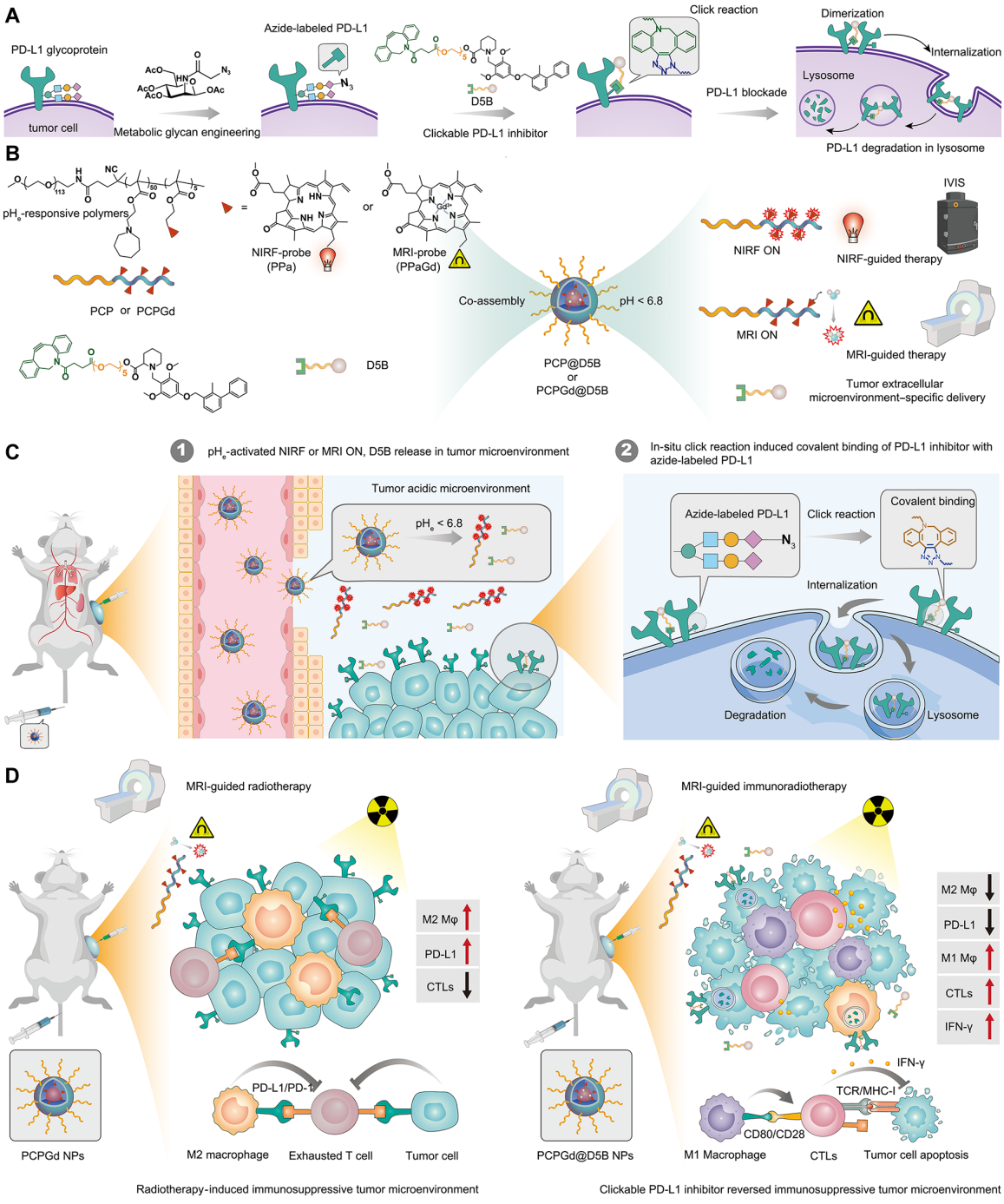


**Fig. 1. Schematic illustration of tumor-specific PD-L1 degradation with the clickable inhibitor for enhancing cancer radioimmunotherapy.** (**A**) The mechanism of click reaction-augmented PD-L1 degradation with the clickable PD-L1 inhibitor. The DBCO-conjugated PD-L1 inhibitor BMS-1 reacts with azide-labeled PD-L1 via click reaction, and BMS-1 subsequently induces PD-L1 dimerization, internalization, and degradation in the lysosome vesicles. (**B**) The clickable PD-L1 inhibitor D5B was co-assembled with a $pH_e$-activatable amphiphilic diblock copolymer (PCP or PCPGd) to form micellar nanoparticles, namely, PCP@D5B or PCPGd@D5B, depending on the type of copolymer used. PCP@D5B or PCPGd@D5B nanoparticles were designed for cancer imaging using near-infrared fluorescence (NIRF)– or magnetic resonance imaging (MRI)–guided therapy and tumor extracellular microenvironment–specific delivery of D5B. (**C**) Mechanism demonstration of PCP@D5B (or PCPGd@D5B)–mediated tumor-selective delivery and release of D5B inhibitor, which degraded PD-L1 on the surface of cell membrane: (1) the nanoparticles dissociated at acidic pH of tumor microenvironment ($pH_e$ < 6.8) to release D5B and turn on the NIRF or MRI probe, and (2) in situ click reaction between D5B and azide-labeled PD-L1 augments PD-L1 degradation on the surface of cell membrane. (**D**) The clickable PD-L1 inhibitor-loaded nanoparticles performed NIRF/MRI-guided RT of tumors and relieved RT-induced immunosuppressive tumor microenvironment (ITM) by degrading PD-L1 on the surface of tumor cells and M2-type tumor-associated macrophage (TAM) membrane, which increased the proportion of M1-type TAMs and activated the tumor-infiltrating CTLs for inhibiting tumor growth and relapse. TCR, T cell receptor; MCH-I, major histocompatibility complex class I.

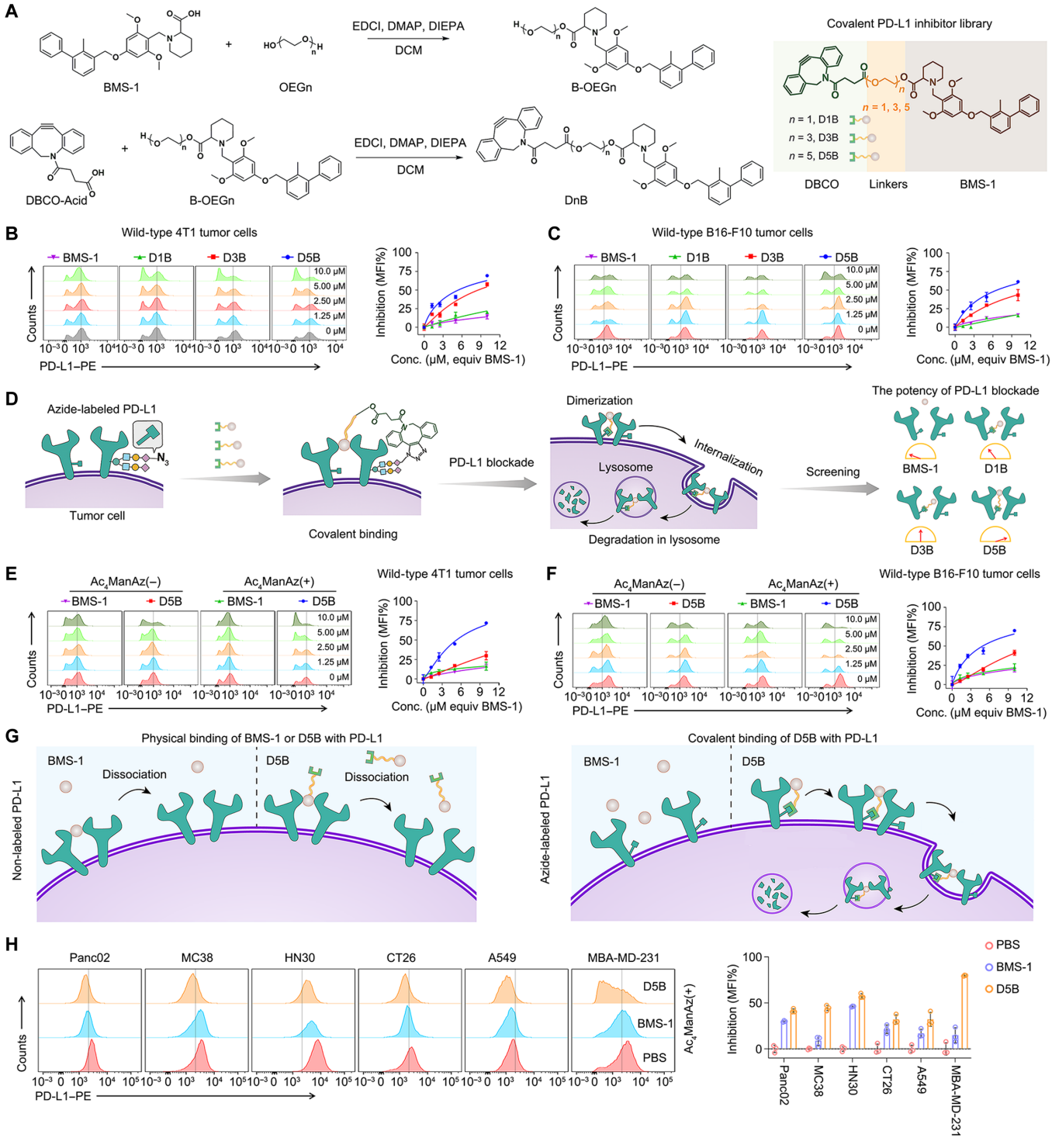


**Fig. 2. The clickable PD-L1 inhibitors degraded PD-L1 on the surface of tumor cell membrane via metabolic glycan engineering and bioorthogonal click chemistry.** (**A**) Synthetic routes of the clickable PD-L1 inhibitors. (**B** and **C**) Flow cytometry examination of PD-L1 abundance and quantification of inhibition efficiency on the membrane surface of (B) wild-type 4T1 tumor cells and (C) wild-type B16-F10 tumor cells [median fluorescence intensity (MFI)]. The tumor cells were first incubated with $Ac_4ManAz$ (25 μM) for 3 days to label PD-L1 with azide groups and then treated with the clickable PD-L1 inhibitors for 24 hour. Last, the PD-L1 abundance on the membrane surface was examined by flow cytometry. (**D**) Schematic illustration of the positive correlation between the OEG linker length of the clickable PD-L1 inhibitors and their PD-L1 degradation efficacy. (**E** and **F**) Flow cytometry–determined PD-L1 abundance on the surface of (E) wild-type 4T1 tumor cells and (F) wild-type B16-F10 tumor cells without or with azide labeling. (**G**) A proposed mechanism for clickable PD-L1 inhibitor–mediated PD-L1 degradation via bioorthogonal click chemistry and metabolic glycan engineering, which is superior over the conventional inhibitors via physical binding. (**H**) Flow cytometry determined the membrane surface PD-L1 degradation profile of the clickable PD-L1 inhibitor in various human and murine tumor cell lines. The data are presented as means ± SD.

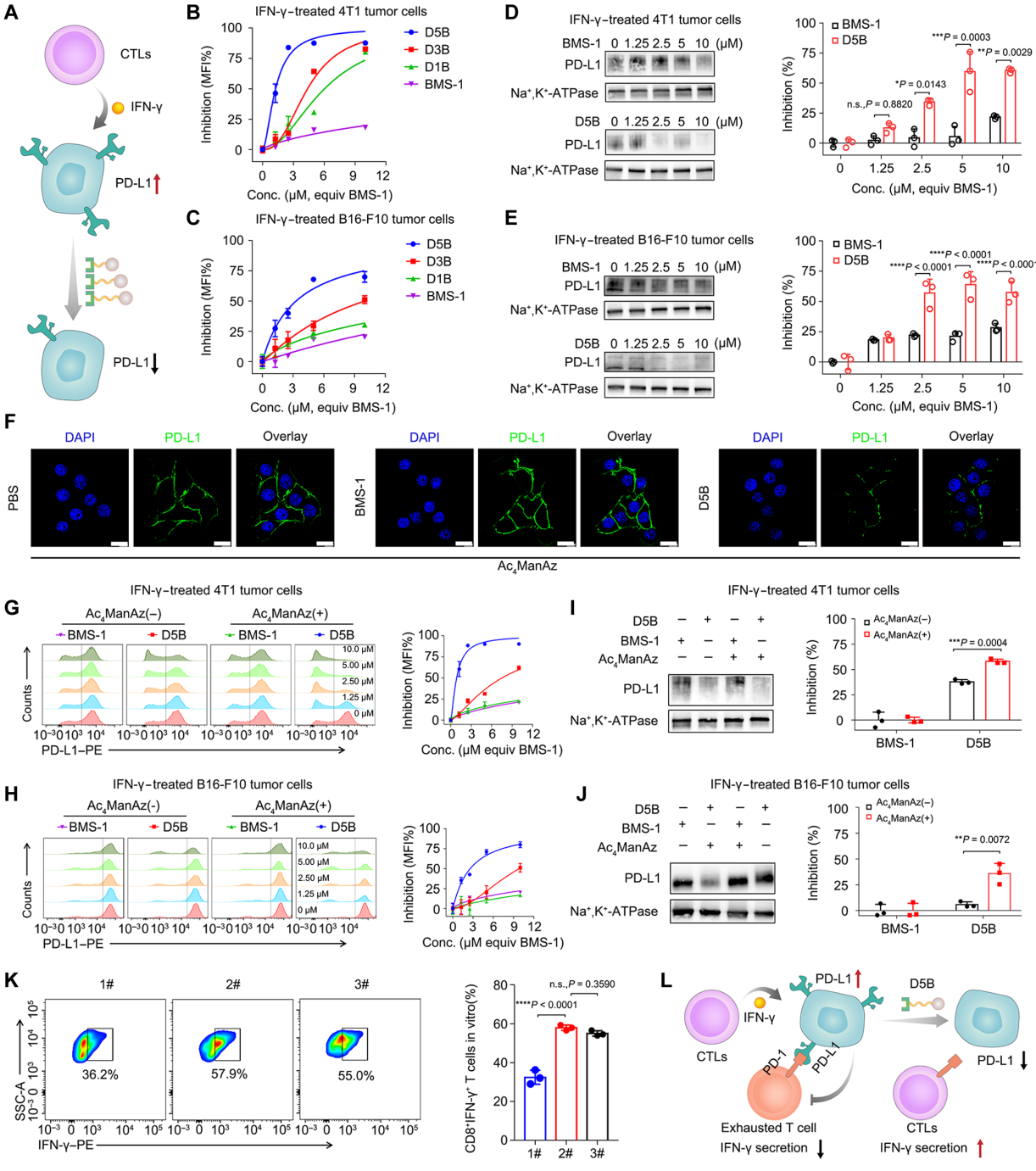


**Fig. 3. The clickable PD-L1 inhibitors highly efficiently abolished IFN-γ–induced PD-L1 expression on the surface of tumor cell membrane.** (**A**) Schematic illustration of IFN-γ–induced PD-L1 up-regulation on the surface of tumor cells in vitro. (**B** to **E**) Flow cytometry and Western blot examination of clickable PD-L1 inhibitor–mediated PD-L1 degradation on the surface of tumor cell membrane in vitro. [(B) and (C)] Flow cytometry detection of PD-L1 abundance on the membrane surface of IFN-γ–pretreated 4T1 (B) and B16-F10 (C) tumor cells. [(D) and (E)] Western blot analysis of PD-L1 abundance on the membrane surface of IFN-γ–pretreated 4T1 (D) and B16-F10 (E) tumor cells. (F) Representative CLSM images of PD-L1 abundance on the membrane surface of 4T1 tumor cells (scale bar = 20 μm). $Na^+,K^+$-ATPase, $Na^+$- and $K^+$-dependent adenosine triphosphatase. (**G** to **J**) Flow cytometry–determined PD-L1 abundance on the membrane surface of IFN-γ–pretreated 4T1 (G) and B16-F10 (H) tumor cells after treatment with 10 μM BMS-1 or D5B. Western blot analysis and semi-quantification of PD-L1 expression on the membrane surface of IFN-γ–pretreated 4T1 (I) and B16-F10 (J) tumor cells with or without azide labeling. (**K**) Representative flow cytometry plots and quantification of IFN-$\gamma^+CD8^+$ T cells. 1#, $CD8^+$ T cells incubated with BMS-1–treated tumor cells; 2#, $CD8^+$ T cells incubated with D5B-treated tumor cells; 3#, $CD8^+$ T cells incubated with PBS. (**L**) Mechanism illustration for PD-L1 degradation increased proliferation of $CD8^+$ T lymphocytes. The data were presented as the means ± SD. *P* values were determined by two-way repeated-measures analysis of variance (ANOVA) with Bonferroni's multiple comparisons test [(D) and (E)], unpaired Student's *t* test [(I) and (J)], or one-way ANOVA with Tukey's multiple comparisons test (L). $^*P < 0.05$, $^{**}P < 0.01$, $^{***}P < 0.001$, and $^{****}P < 0.0001$.

Accordingly, D5B effectively reduced PD-L1 abundance on the surface of azide-labeled tumor cell membrane ($Ac_4ManAz^+$ group) than azide-free tumor cells ($Ac_4ManAz^-$ group) (Fig. 3, G to J, and fig. S8, F to H). These results indicated that the click PD-L1 inhibitor could relieve the acquired immune resistance by inhibiting IFN-γ–upregulated PD-L1 on the surface of tumor cell membrane.

Tumor-infiltrating CTLs are essential for immunological surveillance to eradicate tumor cells. However, tumor cells can inactivate the tumor-infiltrating CTLs via PD-L1 binding with PD-1 expressed on the membrane surface of T lymphocytes (*31*–*35*). We next examined whether PD-L1 inhibition with the clickable PD-L1 inhibitor could reversing tumor cell–mediated inactivation of T lymphocytes (Fig. 3K). $CD8^+$ T cells extracted from the spleen of 4T1 tumor-bearing Balb/c mice were incubated with anti-CD3 and anti-CD28 antibodies. The activated $CD8^+$ T cells were then incubated with pretreated 4T1 tumor cells for 24 hours. Compared to the BMS-1 group, D5B treatment increased the proportion of IFN-$\gamma^+CD8^+$ T cells from 10.2 to 57.9% in a dose-dependent manner (fig. S9). $CD8^+$ T cells incubated with D5B-treated tumor cells showed similar proliferation activity as the native $CD8^+$ T cells in terms of IFN-γ secretion, which was 1.6-fold higher than the fraction of BMS-1–treated group (Fig. 3L). The above data validated that the clickable inhibitor efficiently alleviated the immunosuppression of tumor cells to T lymphocytes by reducing PD-L1 abundance on the surface of tumor cell membrane and thereby blocking the PD-L1/PD-1 interaction in vitro.

### The extracellular tumor acidity-responsive nanoparticles specifically delivered the clickable PD-L1 inhibitor into tumor mass in vivo

PD-L1 expressed on the surface of epithelial cells of the normal organs (e.g., heart and lung) plays a crucial role in maintaining immune homeostasis (*36*). The nonspecific distribution of αPD-L1 or small molecular inhibitors could cause PD-L1 blockade in normal cells, leading to abnormal T cell activation and irAEs (*37*–*40*), suggesting the need for tumor-specific PD-L1 blockade. To achieve tumor-specific delivery of the clickable PD-L1 inhibitor and spatial-confined PD-L1 inhibition in the tumor, two amphiphilic diblock copolymers (i.e., PCH and PDH) sensitively responding to extracellular acidic ($pH_e$ < 6.5 to 6.8) and intracellular acidic ($pH_i$ < 5.0 to 6.0) microenvironment of solid tumors were synthetized via reversible addition-fragmentation chain transfer (RAFT) polymerization. An acid-insensitive analog of PCH and PDH, namely, PBH, was synthesized as the negative control (figs. S10 and S11 and table S2). The above copolymers were further conjugated with a fluorophore pyropheophorbide-a (PPa) or PPaGd [chelated with gadolinium ion ($Gd^{3+}$)] to obtain the PCP (or PCPGd), PDP and PBP diblock copolymers, respectively. The resultant copolymers can self-assemble into spherical micellar nanoparticles for tumor-targeted drug release and (NIRF or MR) imaging–guided RT of tumors.

To investigate acid-triggered nanoparticle disassociation and activation of the NIRFI and MRI signals in vitro, D5B-loaded PCP@D5B, PDP@D5B, or PBP@ D5B nanoparticles with varied acid responsiveness were prepared via a nano-precipitation method (Fig. 4A). Dynamic light scattering (DLS) and transmission electron microscopy (TEM) examinations demonstrated that the $pH_e$-activatable PCP@D5B had a hydrodynamic diameter of ~70 nm at pH 7.4 and disassociated rapidly at pH below 6.5. In contrast, the $pH_i$-responsive PDP@D5B and pH-insensitive PBP@D5B nanoparticles maintained their spherical morphology at both pH 7.4 and 6.5 (Fig. 4B). Fluorescent emission testing revealed that all the three kinds of nanoparticle exhibited quenched fluorescence signal at neutral condition (pH 7.4) due to homo-fluorescence resonance energy transfer effects. In contrast, the PCP@D5B nanoparticles exhibited a sharp fluorescence intensity transition at pH < 6.8 (mimicking $pH_e$), which was ~10-fold higher than that determined at pH 6.5. In addition, fluorescence intensity of the PDP@D5B nanoparticles increased by 10-fold when the buffer pH was declined from 6.5 to 6.0 (mimicking $pH_i$) due to acid-triggered dissociation of the PDP nanoparticles. The fluorescence of the pH-insensitive PBP@D5B nanoparticles kept silent throughout the pH range from 7.4 to 5.8 (fig. S12, A and B).

To demonstrate acid-triggered dissociation and drug release profiles of the D5B-loaded nanoparticles, the PCP@D5B, PDP@D5B, and PBP@D5B nanoparticles were incubated in $pH_e$ and $pH_i$-mimicking phosphate-buffered saline (PBS; pH 5.8 to 7.4). The three types of nanoparticles all showed negligible D5B release upon 1 hour of incubation at pH 7.4 (fig. S12C). In sharp contrast, the PCP@D5B nanoparticles rapidly released over 90% of D5B payload within 30 min of incubation at acidic pH of 6.5 mimicking $pH_e$, and the PDP@D5B comparably released D5B at pH of 6.2 mimicking $pH_i$ (fig. S12D). We next demonstrated $pH_e$-triggered dissociation of the PCP@D5B nanoparticles for extracellular release of the clickable PD-L1 inhibitor D5B. The PCP@D5B, PDP@D5B, and PBP@D5B nanoparticles were pretreated in cell culture medium with pH of 6.5 or 7.4, respectively, for 1 hour and then co-incubated with tumor cells for 5 min at 4°C to prevent cellular uptake of the nanoparticles. CLSM examination revealed negligible fluorescence signal of all three kinds of nanoparticles (red fluorescence assigned to PPa) at pH 7.4 (Fig. 4C). In contrast, when pretreated at pH 6.5, the PCP@D5B group displayed markedly observable fluorescence signal on the surface of tumor cell membrane (green fluorescence) due to $pH_e$-triggered dissociation of the PCP@D5B nanoparticle and physical attachment of the PCP polymer chain onto cell membrane via electrostatic interaction. The above data validated the ability of PCP@D5B nanoparticles for spatially tunable drug release outside the tumor cells by precisely responding to $pH_e$ of the solid tumors.

To demonstrate $pH_e$-triggered D5B release from the PCP@D5B nanoparticles and its covalent binding onto the surface of cell membrane via biorthogonal click reaction in vitro, the three types of nanoparticles were loaded with the DBCO-FITC conjugate (termed as $DBCO^{FITC}$) and incubated with azide-labeled 4T1 tumor cells at acidic or neutral pH condition (e.g., pH 6.5 or 7.4). Upon 30 min of incubation at 4°C, the cells were washed with PBS at pH 6.5 to remove all the nanoparticles or dissociated copolymers. Flow cytometry and CLSM examination displayed distinct green fluorescence signal of FITC on the surface of 4T1 cell membrane in the PCP@$DBCO^{FITC}$ (pH 6.5) group. In contrast, no observable fluorescence signal was found at neutral pH of 7.4 or in the PDP@$DBCO^{FITC}$ and PBP@$DBCO^{FITC}$ groups disregarding the pH conditions (pH 7.4 or 6.5) (fig. S12E). This confirmed that the PCP@D5B nanoparticles selectively released DBCO-FITC at $pH_e$ condition for covalently labeling of PD-L1 on the surface of tumor cells via click chemistry.

To elucidate the importance of the PCP@D5B nanoparticles for extracellular release of the clickable D5B inhibitor, we investigated their PD-L1 degradation profiles in 4T1 tumor cells in vitro (Fig. 4D). Flow cytometry examination displayed that free D5B inhibited over 90% of PD-L1 abundance on the surface of cell membrane at both

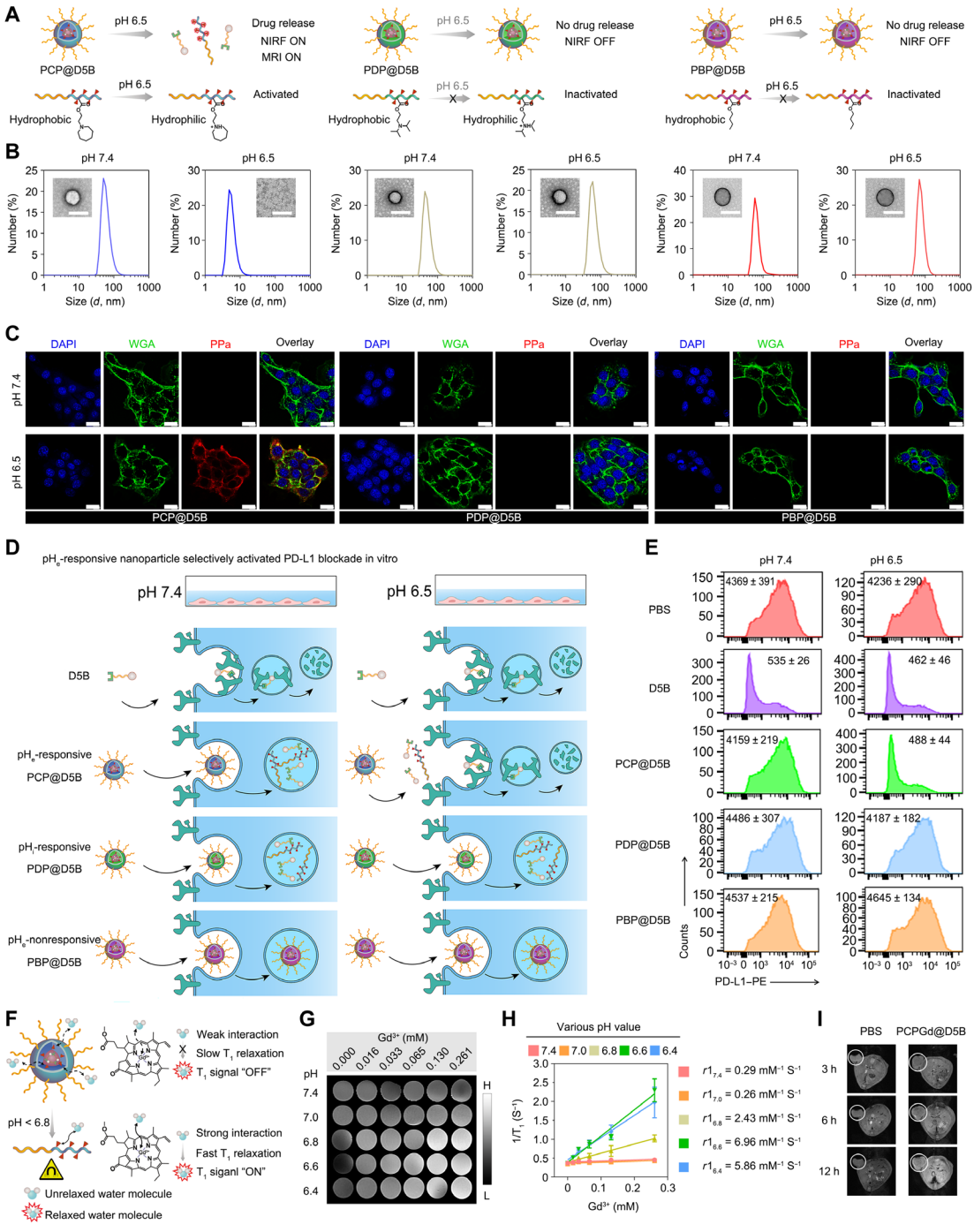


**Fig. 4. Engineering and characterization of the $pH_e$-activatable PCP@D5B nanoparticles for tumor-targeted delivery of the clickable PD-L1 inhibitor and NIRF/MR imaging–guided cancer therapy.** (**A**) Acid-responsive mechanism illustration of the $pH_e$-activatable PCP@D5B, $pH_i$-activatable PDP@D5B, and pH-inactivated PBP@D5B nanoparticles for acid-triggered nanoparticle dissociation and activation of NIRF/MRI signals. (**B**) Dynamic light scattering (DLS)– and transmission electron microscopy (TEM)–determined particle size distribution and morphology change of the PCP@D5B, PDP@D5B, and PBP@D5B nanoparticles at pH 7.4 and 6.5, respectively (scale bars, 100 nm). (**C**) Representative CLSM images of cell membrane [wheat germ agglutinin (WGA), green] and colocalization with PPa-labeled nanoparticles (red) at the predesignated time points. 4T1 tumor cells were incubated with PCP@D5B, PDP@D5B, or PBP@D5B nanoparticles for 5 min under different pH conditions (scale bars, 20 μm). (**D**) Schematic illustration for PCP@D5B-performed PD-L1 degradation on the surface of tumor cell membrane by specifically releasing D5B payload at the extracellular acidic microenvironment in vitro. (**E**) Flow cytometry analysis of PD-L1 abundance on the surface of 4T1 tumor cell membrane; inset number represents the MFI values. (**F**) The mechanism of pH-activated NIRF and MRI signals of PCPGd@D5B nanoparticles. (**G**) Representative $T_1$ maps of PCPGd@D5B nanoparticles determined at varied pH values. (**H**) The longitudinal relaxation rate ($r_1$) versus $Gd^{3+}$ concentration determined at different pH values. (**I**) MRI of 4T1 tumor-bearing mice in vivo. The mice were intravenously injected with PBS or PCPGd@D5B nanoparticles at a $Gd^{3+}$ dose of 1.5 mg/kg and then imaged at the predetermined intervals (white circles represent the tumors). The data are presented as the means ± SD. h, hours.

pH 7.4 and 6.5. In contrast, at pH of 6.5 mimicking $pH_e$, the D5B was released from the PCP@D5B nanoparticles and comparably reduced PD-L1 abundance on the surface of cell membrane as free D5B, which was 10-fold more efficient than that determined at pH of 7.4. It was worth noting that D5B encapsulated inside the PDP@D5B and PBP@D5B nanoparticles marginally affected PD-L1 abundance at either pH 7.4 or pH 6.5, although the D5B can be released in the acidic lysosomal vesicles upon intracellular uptake of the nanoparticles (Fig. 4E). These data validated that the crucial importance of spatially confined delivery of D5B to the extracellular tumor milieu for efficient PD-L1 degradation.

To further exploit the potential of the PCP@D5B nanoparticles for NIFI/MRI-guided therapy of cancer, the nanoparticles integrating a $Gd^{3+}$-based MRI tracer (namely, PCPGd@D5B) were engineered, which displayed obviously enhanced $T_1$-weighted MR signal and decreased $T_1$ relaxation time at pH < 6.8 (Fig. 4, F and G, and fig. S12F), which was attributed to acid-triggered dissociation of the nanoparticles for exposing $Gd^{3+}$ to the aqueous environment. The normalized $T_1$ MR signals of PCPGd@D5B markedly increased by ~24-fold when the pH values decreased from 7.4 to 6.6 mimicking $pH_e$ (Fig. 4H). Compared to that of the PBS group, the tumor tissue displayed enhanced $T_1$-weight MR signal of the PCPGd@D5B group (Fig. 4I), verifying the ability of the PCPGd@D5B nanoparticles for dual-model (NIF and MR) imaging–guided cancer therapy.

### Tumor-specific delivery of the clickable inhibitor efficiently degraded PD-L1 and regressed tumor growth in vivo

Given the satisfying performance of the PCP@D5B nanoparticles for $pH_e$-triggered release of the clickable PD-L1 inhibitor in vitro, we next evaluated their ability for tumor-targeted delivery of the D5B inhibitor and spatially confined PD-L1 degradation in the tumor tissue in vivo. To this end, we established a subcutaneous 4T1 tumor model in BALB/c mice (Fig. 5A and fig. S13A). The D5B-loaded PBP@D5B, PDP@D5B, and PCP@D5B nanoparticles were intravenously injected into the tumor-bearing mice. In vivo imaging system (IVIS) fluorescence imaging in vivo demonstrated markedly higher fluorescence signal in the tumor tissue of the PCP@D5B group compared to that of the PDP@D5B and PBP@D5B groups within 12 hours after nanoparticle administration. The fluorescence signal of the PDP@D5B group increased gradually 12 hours after administration, while the PBP@D5B nanoparticles remained silent. This phenomenon verified that, upon intratumoral accumulation, the PCP@D5B nanoparticles were rapidly activated in the extracellular milieu to generate fluorescence signal of PPa. In contrast, the intratumorally distributed PDP@D5B nanoparticles were slowly internalized into tumor cells and dissociated inside the endosomes or lysosome vesicles for fluorescence activation (Fig. 5, B and C, and fig. S13, B to D). Above data validated the ability of the PCP@D5B nanoparticles for extracellular dissociation and release of the D5B payload.

We then analyzed the pharmacokinetic profiles and biodistribution of D5B administrated in free form or delivered with the micellar nanoparticles. Upon intravenous administration into the 4T1 tumor-bearing Balb/c mice, all nanoparticle formulations showed >2-fold longer blood clearance half-life ($t_{1/2\beta}$) than free D5B, verifying the nanoparticle formulations elongated the blood circulation of the clickable inhibitor D5B (Fig. 5D). Quantitation assay further validated higher D5B accumulation at the tumor site of PCP@D5B group in the first 8 hours after nanoparticle injection, whereas the comparable intratumoral D5B concentration was found in the PBP@D5B and PDP@D5B groups at 24 hours after administration (Fig. 5E and fig. S13E). These results demonstrated that the $pH_e$-activatable PCP@D5B nanoparticles could facilitate small molecular drug delivery to the solid tumor in vivo.

We next investigated the antitumor performance of the D5B-loaded micellar nanoparticles in mouse models of 4T1 breast and B16-F10 melanoma tumors in vivo (Fig. 5F). Notably, the PCP@D5B nanoparticles highly efficiently inhibited over 60% of 4T1 tumor growth and elongated the half survival date of 4T1 tumor-bearing mice to over 50 days. However, the PDP@D5B and PBP@D5B nanoparticles negligibly affected 4T1 tumor growth despite both of them efficiently delivered D5B into the tumor mass comparable to the PCP@D5B ones (Fig. 5, G and H, and fig. S14). Immunohistochemical (IHC) staining of the tumor sections and flow cytometry examination in vivo validated that PCP@D5B treatment considerably decreased PD-L1 abundance at the end of antitumor study (Fig. 5, I and J, and fig. S15A). In contrast, the D5B, PDP@D5B, and PBP@D5B groups all exhibited comparable PD-L1 abundance as that of the PBS group. This phenomenon could be explained by the poor tumor-selective distribution of free D5B and ineffective extracellular D5B release profile of the PDP@D5B PBP@D5B nanoparticles in vivo. Together, the above data validated the superior antitumor performance of the PCP@D5B nanoparticles could be attributed to their ability to efficiently reduce PD-L1 abundance in the tumor tissues in vivo.

To determine the mechanism underlying the superior antitumor performance of the PCP@D5B nanoparticles, we evaluated the antitumor immune response in 4T1 tumor-bearing mouse model. PCP@D5B treatment induced 2.0-fold higher dendritic cell (DC) maturation in the tumor-draining lymph nodes (TDLNs) compared to all other groups (fig. S15B). Flow cytometry examination revealed that PCP@D5B treatment noticeably recruited tumor-infiltrating $CD8^+$ T cells compared to the PBS group (Fig. 5, K and L, and fig. S15, C and D). For instance, the PCP@D5B displayed 3.7- and 8.2-fold higher tumor mass–normalized numbers of tumor-infiltrating $CD8^+$ and IFN-$\gamma^+CD8^+$ T cell, respectively, than that of the PBS group. However, free D5B, the PDP@D5B and PBP@D5B nanoparticles all marginally increased tumor-infiltrating $CD8^+$ and IFN-$\gamma^+CD8^+$ T cells (Fig. 5, M and N). Cytokine IFN-γ plays critical roles in regulating cellular immune response (*41*). Compared to the PBS group, enzyme-linked immunosorbent assay (ELISA) measurement at 3 days after treatment further determined increased intratumoral secretion of IFN-γ in the PCP@D5B group (Fig. 5O). IHC staining and semiquantitative analysis revealed comparable PD-L1 expression profiles in the major organs (e.g., heart, liver, spleen, lung, and kidney) of the PCP@D5B and PBS groups (Fig. 5P and fig. S15E), implying good biosafety of the PCP@D5B nanoparticles to avoid nonspecific PD-L1 blockade in the normal tissues (Fig. 5Q). These findings collectively verified that PCP@D5B elicited antitumor effects in 4T1 tumors by specific degrading PD-L1 of tumor tissue in vivo.

### The clickable PD-L1 inhibitor boosted antitumor efficacy of RT and elicited immunological memory to prevent tumor metastasis

RT is one of the primary modalities for malignant tumor therapy (*42*–*44*). Recent clinical investigations had demonstrated that RT could enforce ICB therapy by promoting DC maturation, priming $CD8^+$ T cells in the TDLNs, and enhancing $CD8^+$ T cell response in the tumor microenvironment (*45*, *46*). However, RT obviously upregulates PD-L1 expression on the surface of tumor cells and recruits

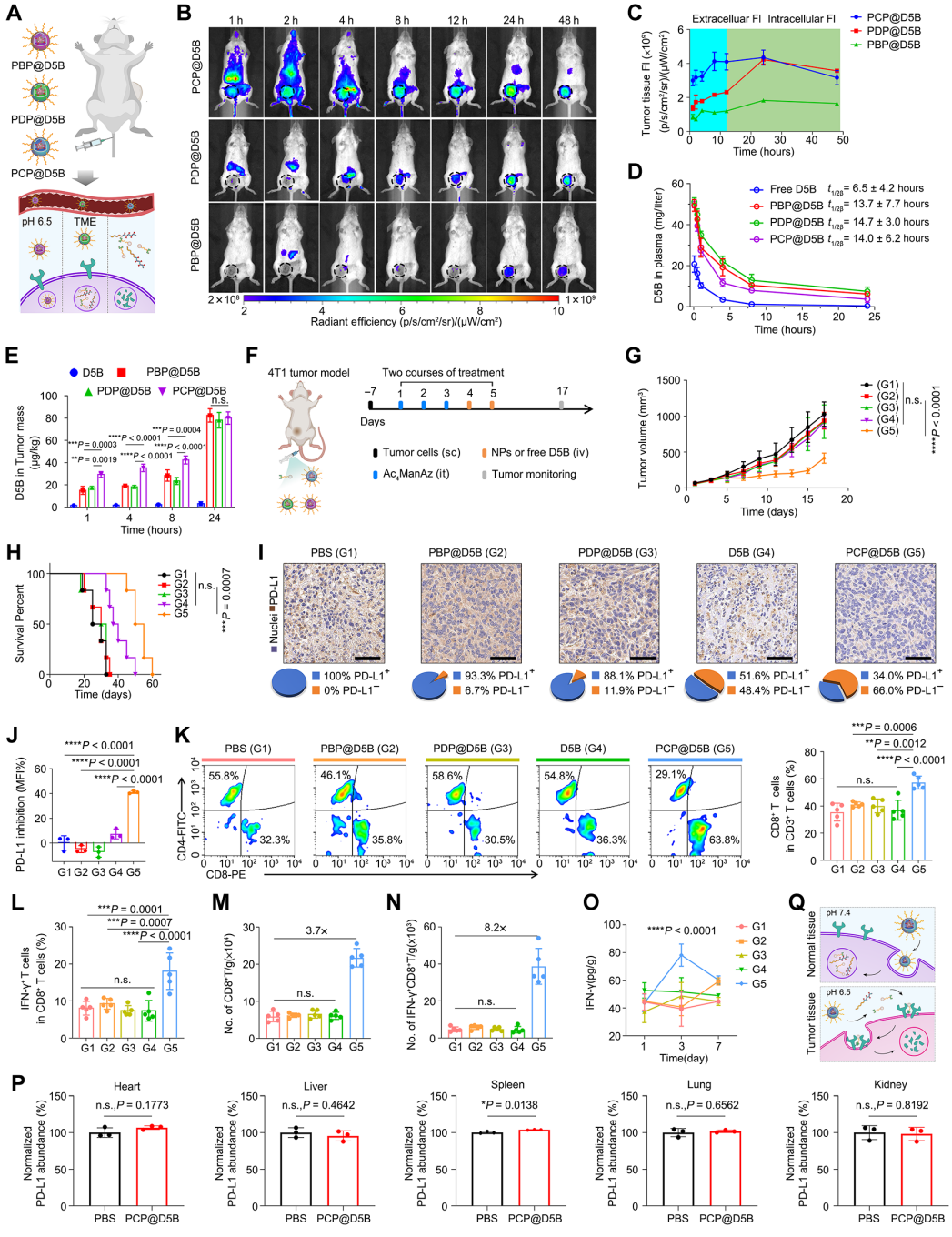


**Fig. 5. The $pH_e$-activatable PCP@D5B nanoparticles efficiently degraded PD-L1 and regressed 4T1 tumor growth in vivo.** (**A**) Schematic illustration of pH-triggered extracellular delivery of D5B for PD-L1 degradation. (**B**) Representative IVIS fluorescence images of 4T1 tumor-bearing BALB/c mice in vivo. (**C**) Semiquantitative of PPa fluorescence intensity from (B) ($n = 3$ mice). (**D**) High-performance liquid chromatography (HPLC)–determined pharmacokinetics of D5B-loaded PCP@D5B, PDP@D5B, and PBP@D5B nanoparticles or free D5B ($n = 3$ mice). (**E**) HPLC-determined D5B distribution in the tumor mass after intravenous injection ($n = 3$ mice). (**F**) Experimental schedule for antitumor study in vivo. it, intratumoral; iv, intravenous; sc, subcutaneous. (**G** and **H**) Averaged tumor growth curves (G), and (H) animal survival curves of 4T1 tumor-bearing mice (n = 6 mice). (**I** and **J**) Immunohistochemical (IHC) (I) and flow cytometry (J) examination of PD-L1 abundance 3 days after treatment ($n = 3$ mice; scale bars, 50 μm). (**K**) Flow cytometry examination of tumor-infiltrating $CD8^+$ and $CD4^+$ T cells (gated on $CD3^+CD45^+$) ($n = 5$ mice). (**L**) Flow cytometry examination of tumor-infiltrating IFN-$\gamma^+CD8^+$ T cells (n = 5 mice). (**M** and **N**) Tumor mass normalized number of tumor-infiltrating $CD8^+$ (M) and IFN-$\gamma^+CD8^+$ T cells (N) ($n = 5$ mice). (**O**) Enzyme-linked immunosorbent assay (ELISA) analysis of intratumoral IFN-γ cytokine secretion at 1, 3, and 7 days after treatment ($n = 3$ mice). (**P**) IHC examination of PD-L1 abundance in the normal tissue 3 days after the treatment. (**Q**) Schematic description for tumor-specific delivery of D5B and PD-L1 inhibition with the $pH_e$-activatable nanoparticles. All data are presented as the means ± SD. *P* values were determined by one-way ANOVA with Tukey's post hoc test [(J) to (N)], repeated-measures two-way ANOVA with Tukey's multiple comparisons test [(E), (G), and (O)], log-rank test (H), or unpaired Student's *t* test (P). $^*P < 0.05$, $^{**}P < 0.01$, $^{***}P < 0.001$, and $^{****}P < 0.0001$. n.s., not significant.

the immunosuppressive immune cells like M2-type TAMs (*47*, *48*). PD-L1 on the surface of TAM membrane hampers the antitumor immune response of CTLs through the PD-1/PD-L1 axis (*49*–*51*). Thus, it is crucial to block PD-L1 on the surface of tumor cells and TAM membrane for counteracting RT-induced ITM.

We first demonstrated that RT efficiently elicited ICD of tumor cells by promoting calreticulin exposure on the membrane and extracellular efflux of high mobility group box 1 in vitro (fig. S16). We next investigated the antitumor efficacy of combination therapy by PCPGd@D5B + RT in vivo. Under the guidance of MRI, subcutaneous 4T1 tumors were treated with RT at 6.0 gray (Gy) when the tumor volume reached 50 $mm^3$ (Fig. 6A). RT initially inhibited tumor growth, followed by accelerated tumor progression in all mice at 30 days after treatment. In sharp contrast, PCPGd@D5B + RT treatment completely eradicated 50% of the tumor xenografts, with 60% of the tumor-bearing mice survived over 100 days (Fig. 6, B and C). Mechanistic study of the antitumor immunity revealed that RT considerably induced DCs ($CD11c^+CD80^+CD86^+$) maturation in the TDLNs compared to the control groups when determined 3 days after treatment (Fig. 6D and fig. S17A). Flow cytometry examination further revealed that combinatory therapy by PCPGd@D5B + RT markedly increased the percentage of tumor-infiltrating IFN-$\gamma^+CD8^+$ T cells (Fig. 6, E and F, and fig. S17, B and C) compared to the RT (PCPGd + RT) and PCPGd@D5B groups (Fig. 6, G to I).

It was worth noting that PCPGd + RT treatment increased the fraction of M2-like TAMs ($CD206^+CD86^-$). In contrast, the PCPGd@D5B and PCPGd@D5B + RT groups displayed highly increased proportion of M1-like TAMs ($CD206^-CD86^+$) (fig. S17, D and E), suggesting a tumor-suppressive microenvironment (Fig. 6J). In addition, we observed that PCPGd + RT treatment up-regulated PD-L1 expression in tumor compared to the PBS. In contrast, the PCPGd@D5B and PCPGd@D5B + RT groups displayed much lower PD-L1 abundance on the membrane surface (Fig. 6K and fig. S17, F and G). Together, these findings demonstrated that PCPGd + RT recruited M2-TAMs and up-regulated PD-L1 abundance in tumors, resulting in adaptive immune evasion to facilitate tumor growth. However, the combination of PCPGd@D5B + RT efficiently provoked an adaptive antitumor immune response for tumor regression in vivo.

To evaluate whether combinatory therapy by PCP@D5B + RT elicited systemic antitumor immune response, we established an abscopal 4T1 tumor model. Upon intravenous injection of the D5B-free PCPGd or D5B-loaded PCPGd@D5B nanoparticles, the primary tumors were treated with x-ray irradiation at 6.0 Gy (Fig. 6L). Compared to the PCPGd + RT and PCPGd@D5B groups, combination therapy by PCPGd@D5B and RT completely eradicated the primary tumors and regressed the abscopal tumors, with 80% of the tumor-bearing survived over 50 days (Fig. 6, M and N, and fig. S17H). In contrast, despite monotherapy by RT alone (the PCPGd + RT group) or PCPGd@D5B nanoparticles highly efficiently inhibited primary tumor growth, they marginally delayed abscopal tumor growth and elongated the median survival of the tumor-bearing mice.

To validate elicitation of the systemic antitumor immune response, we analyzed tumor-infiltrating $CD8^+$ T cells in the abscopal tumor residuals. Combination therapy by PCPGd@D5B + RT remarkably increased the tumor-infiltrating $CD8^+$ T cells in the abscopal tumor compared to the PCPGd@D5B or RT groups (Fig. 6O and fig. S17, I and J). Flow cytometry examination further revealed that PCPGd@D5B + RT treatment efficiently activated effector memory T cells ($CD8^+CD44^+CD62L^-$, $T_{EM}$ cells) in the spleen 14 days after treatment. In particular, the mice of the PCPGd@D5B + RT group exhibited fourfold higher $T_{EM}$ proportion compared to those of the PBS and RT groups (Fig. 6P). The activation of immunological memory was further validated in lung metastasis tumor model of 4T1 breast tumor. The PCPGd@D5B + RT treatment markedly inhibited lung metastasis of intravenously injected 4T1 tumor cells (Fig. 6Q). Together, these results confirmed that the combination of PD-L1 degradation with the PCPGd@D5B nanoparticles and RT elicited systemic immune response to inhibit both the primary and abscopal 4T1 tumors and induced immunological memory to prevent lung metastasis of intravenously injected tumor cells (Fig. 6R).

### The clickable PD-L1 inhibitors potentiated radioimmunotherapy by relieving RT-induced immune evasion of B16-F10 melanoma tumor in vivo

We further evaluated whether the clickable PD-L1 inhibitors augment the antitumor immune response of RT by overcoming the acquired immune resistance in B16-F10 tumor model (Fig. 7A). Compared to the PBS group, PCPGd + RT or PCPGd@D5B displayed moderate tumor growth inhibition rate of 50%. In contrast, the combination of PCPGd@D5B + RT suppressed 95% of tumor growth, with complete tumor elimination in 43% of the tumor-bearing mice and elongated survival time over 50 days (Fig. 7, B and C).

To explore the underlying mechanism for enhanced antitumor performance of the PCPGd@D5B + RT group, we analyzed DC ($CD11c^+CD80^+CD86^+$) maturation in the TDLNs 3 days after the final treatment. PCPGd@D5B + RT strongly elicited DC maturation compared to PBS (Fig. 7, D and E). The fraction of M2-type TAMs ($CD206^-CD80^+$) markedly declined and M2 to M1 TAMs ratio increased in the PCPGd@D5B and PCPGd@D5B + RT groups (Fig. 7, F to H, and fig. S18A). Furthermore, combination therapy by PCPGd@D5B + RT effectively suppressed PD-L1 expression on the surface of tumor cells and TAM membrane compared to the PCPGd + RT group (Fig. 7, I and J, and fig. S18, B and C), verifying that D5B abolished RT-elicited PD-L1 expression.

The combination of PCPGd@D5B + RT efficiently promoted 2.0-fold more tumor-infiltrating $CD8^+$ T cell compared to the PCPGd + RT group (Fig. 7, K to M, and fig. S18D). Immunofluorescence staining of the tumor sections confirmed that PCPGd@D5B + RT effectively reduced PD-L1 abundance on the membrane surface of both tumor cells and TAMs, thereby facilitating intratumoral infiltration of $CD8^+$ T cells (Fig. 7N). Although RT effectively eliminate B16-F10 tumor xenografts, it up-regulated PD-L1 expression and recruited M2-like TAMs, which caused adaptive immune resistance (Fig. 7O). These findings collectively indicated that the clickable PD-L1 inhibitor efficiently inhibited PD-L1 of tumor cells and TAMs to ameliorate RT-induced immune evasion.

It was reported that antibody-based ICB therapy suffers from a moderate response rate in clinic due to insufficient tumor-specificity and poor tumor permeability of the antibody therapeutics (*52*, *53*). The antitumor efficacy of PCP@D5B and αPD-L1 was therefore compared in a B16-F10 tumor-bearing mouse model in vivo. Compared to αPD-L1, the PCP@D5B nanoparticles much more efficiently inhibited tumor growth (fig. S19, A and B), and prolongated half survival of the tumor-bearing mice to 45 days. However, all mice of the αPD-L1 group lost in 40 days after treatment (fig. S19C), validating the advantage of the PCPGd@D5B nanoparticles over αPD-L1 for tumor-specific delivery of the clickable inhibitor and spatial-confined PD-L1 degradation in vivo. In addition, we compared the antitumor

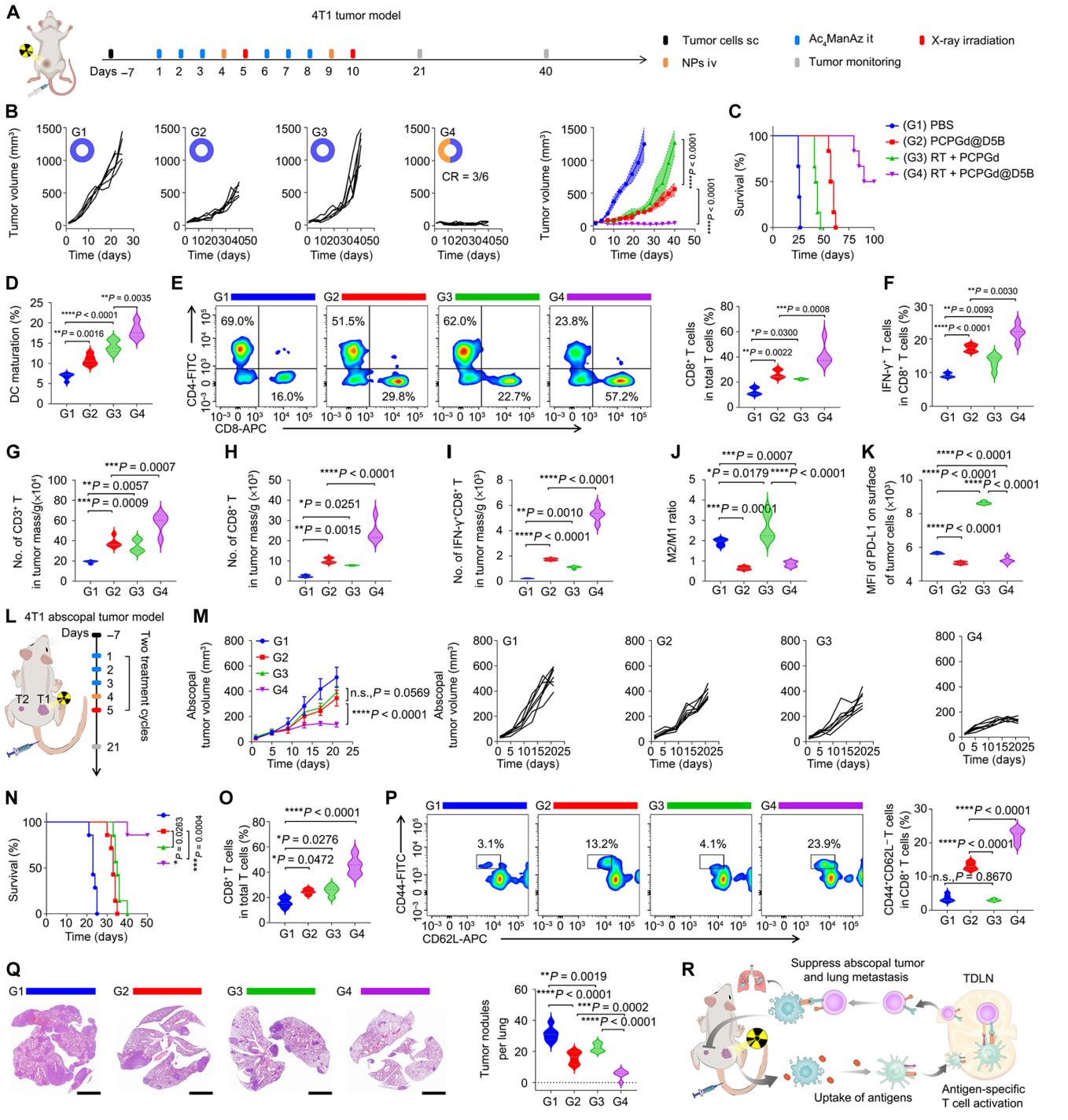


**Fig. 6. Combinatory therapy of the PCPGd@D5B nanoparticles and RT suppressed abscopal 4T1 tumor growth and lung metastasis in vivo.** (**A**) Treatment schedule of in 4T1 tumor model in vivo. (**B**) Individual 4T1 tumor growth curves [complete regression (CR)] ($n = 6$ mice). (**C**) Survival rates of 4T1 tumor-bearing mice. (**D**) Flow cytometry analysis of $CD86^+CD80^+$ DCs ($n = 3$ mice). (**E**) Flow cytometry examination of tumor-infiltrating $CD8^+$ and $CD4^+$ T cells, and (**F**) IFN-$\gamma^+CD8^+$ T cells ($n = 5$ mice). (**G** to **I**) Absolute numbers of tumor-infiltrating $CD3^+$ (G), $CD8^+$ (H), and IFN-$\gamma^+CD8^+$ (I) T cells after the indicated treatments ($n = 5$ mice). (**J**) M2/M1 ratio after treatment ($n = 5$ mice). (**K**) Flow cytometry–determined PD-L1 abundance on the surface of tumor cells membrane ($n = 5$ mice). (**L**) Treatment schedule of 4T1 abscopal tumor model (T1 and T2 represents the primary and abscopal tumors, respectively). (**M**) Averaged tumor growth curves ($n = 6$ mice), and (**N**) Survival rates of the mice ($n = 6$ mice). (**O**) Flow cytometry–determined tumor-infiltrating $CD8^+$ T cells. (**P**) Flow cytometry analysis of $T_{EM}$ cells ($CD62L^-CD44^+$) in the spleens of 4T1 tumor-bearing mice ($n = 5$ mice). (**Q**) Hematoxylin and eosin staining and quantification of metastatic tumor lesions in the lung ($n = 6$ mice; scale bars, 2.5 mm). (**R**) Mechanism illustration for combinatory therapy–elicited antitumor immunity and immunological memory to suppress abscopal tumor and lung metastases. The data are presented as the means ± SD. *P* values were determined by repeated-measures two-way ANOVA with Tukey's multiple comparisons test [(B) and (M)], log-rank test [(C) and (N)], or one-way ANOVA with Tukey's post hoc test [(D) to (K) and (O) to (Q)]. $^*P < 0.05$, $^{**}P < 0.01$, $^{***}P < 0.001$, and $^{****}P < 0.0001$.

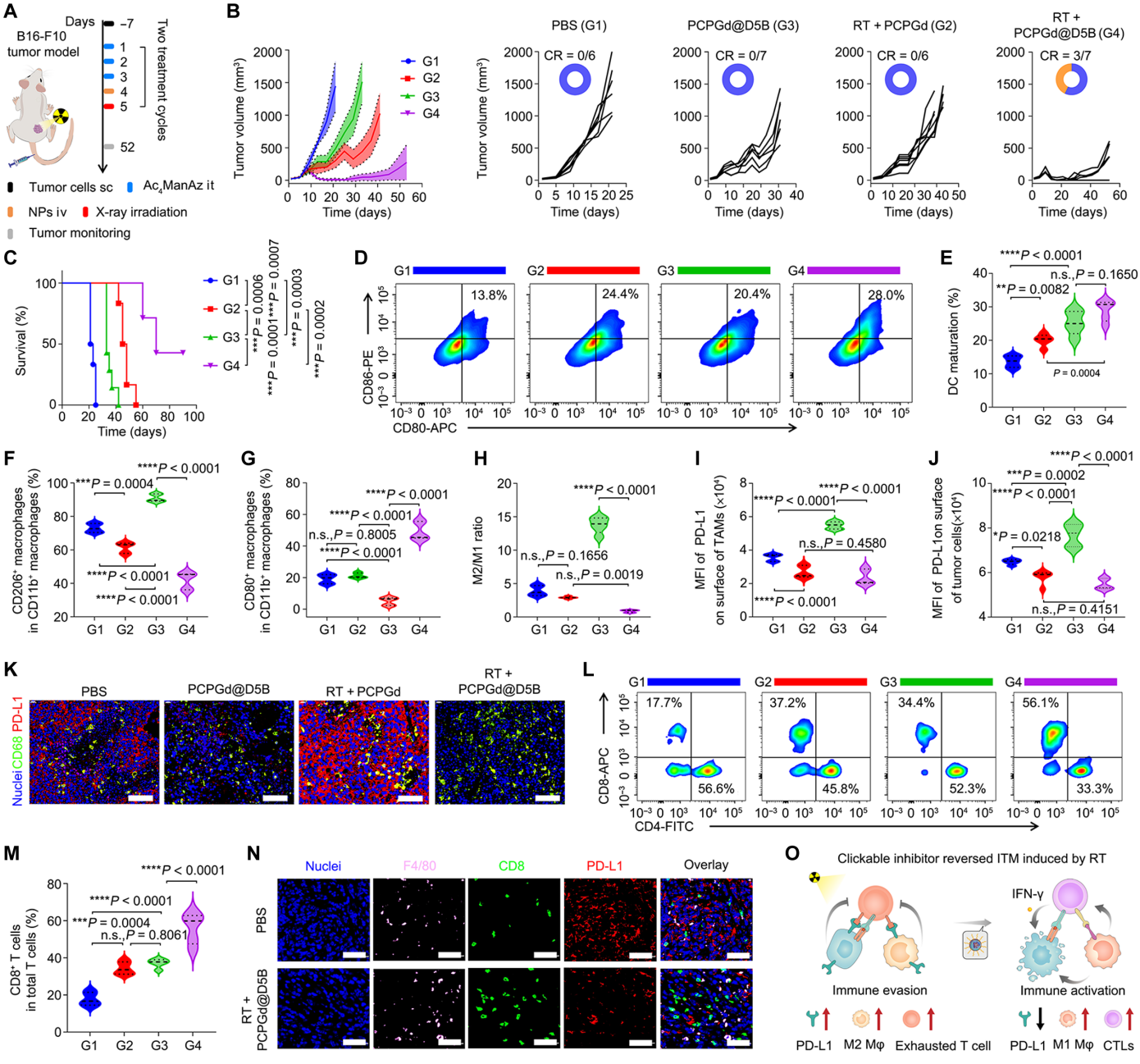


**Fig. 7. The $pH_e$-activatable PCPGd@D5B nanoparticles enforced radioimmunotherapy by reversing RT-induced immune evasion in B16-F10 tumors in vivo.** (**A**) Treatment schedule for the antitumor study in B16-F10 tumor-bearing mice in vivo. (**B**) The averaged and individual B16-F10 tumor growth curves, and (**C**) survival curves of B16-F10 tumor-bearing mice monitored during the therapy period (CR represents the fractions of complete tumor regression at the end of antitumor study, $n = 6$ or 7 mice). (**D** and **E**) Representative flow cytometry plots (D), and quantification data of $CD86^+CD80^+$ DCs (E) ($n = 3$ mice). (**F** and **G**) Flow cytometry–determined fractions of (F) M2-phenotype ($CD11b^+CD206^+$) and (G) M1-phenotype ($CD11b^+CD80^+$) TAMs ($n = 5$ mice). (**H**) The M2/M1 ratio of TAMs. (**I** and **J**) The MFIs of PD-$L1^+$ TAMs ($CD11b^+CD80^+$) (I), and PD-$L1^+CD45^-$ tumor cells (J) after treatment. (**K**) Immunofluorescence staining and semi-quantitation of PD-$L1^+$ TAMs in the tumor sections (scale bars, 40 μm). (**L** and **M**) Representative flow cytometry plots (L) and quantification (M) of tumor-infiltrating $CD8^+$ and $CD4^+$ T cells (gated on $CD45^+CD3^+$) ($n = 5$ mice). (**N**) Immunofluorescence staining and semi-quantitation of PD-$L1^+$ TAMs, and $CD8^+$ T cells in the tumor sections (scale bars, 40 μm). (**O**) Schematic illustration of the clickable PD-L1 inhibitor mitigated the acquired immune evasion. RT induces ITM by up-regulating PD-L1 and recruiting M2-type TAMs, which was reversed with the clickable PD-L1 inhibitor through degrading PD-L1 on the surface of tumor cell membrane and repolarizing M2-type TAMs to M1 type. The data are presented as the means ± SD. *P* values were determined by repeated-measures two-way ANOVA with Tukey's multiple comparisons test (B), log-rank test (C), or one-way ANOVA with Tukey's post hoc test [(E) to (J) and (M)], $^*P < 0.05$, $^{**}P < 0.01$, $^{***}P < 0.001$, and $^{****}P < 0.0001$.

performance of PCP@D5B + RT with that of αPD-L1 + RT in the mouse model of B16-F10 melanoma tumor. The combination of αPD-L1 + RT also moderately suppressed tumor growth in four of the five mice. In contrast, PCPGd@D5B + RT completely suppressed tumor growth in all mice, which was more efficient than the αPD-L1 + RT group (fig. S19, D and E). Mechanistic study of the antitumor immunity revealed that PCPGd@D5B + RT much more efficiently increased tumor-infiltrating $CD8^+$ T cells compared to αPD-L1 or αPD-L1 + RT (fig. S19, F and G). In addition, we observed PD-L1 up-regulation on the surface of tumor cell membrane receiving αPD-L1 + RT treatment compared to the PBS group. In contrast, the PCPGd@D5B + RT group displayed reduced PD-L1 expression in the tumor tissues (fig. S19H). Flow cytometry examination and immunofluorescent staining further validated that PCPGd@D5B + RT increased the tumor-infiltrating $CD8^+$ T cells and reduced PD-L1 abundance, compared to αPD-L1 + RT (fig. S19, I and J). Together, these results confirmed that the combination of clickable PD-L1 inhibitor with RT much more efficiently elicited antitumor immunity in B16-F10 tumor-bearing mice compared to αPD-L1 + RT. The body weights of all the animals increased gradually (fig. S20, A to E). Histological analysis at the end of the antitumor study displayed negligible histopathological damage of the major organs (fig. S20F), suggesting favorable biosafety of D5B-loaded nanoparticles.

## DISCUSSION

The interaction between immune checkpoints PD-L1 and PD-1 can inactivate the CTLs and lead to immune evasion. ICB therapy blocking the PD-L1/PD-1 axis has been clinically approved for immunotherapy of various tumors. However, current antibody-based ICB therapy suffers from limited tumor permeability and on-target but off-tumor distribution pattern of αPD-L1. Furthermore, antibody-based immune checkpoint inhibitors (e.g., αPD-L1) generally displayed elongated blood circulation time than the small molecular counterparts. It is hard to adjust the antibody dose when the irAEs occurs. Despite that small-molecule PD-L1 inhibitors were exploited in past years to combat the disadvantages of antibody-based inhibitors, clinical translation of these small molecular candidates is hampered by their low PD-L1 binding affinity and insufficient tumor-specific distribution. To address above challenges, we rationally screened out a clickable PD-L1 inhibitor D5B by taking advantages of the metabolic glycan engineering and bioorthogonal click chemistry. Furthermore, achieving spatially confined PD-L1 degradation in the pathological cues of solid tumors, a $pH_e$-activatable nanoplatform was further used for tumor-targeted delivery of the clickable PD-L1 inhibitor. The $pH_e$-activatable nanoparticles designed for D5B delivery remain inactive in the normal physiological environment while being specifically activated in the acidic extracellular tumor microenvironment for payload release.

Elucidating the structure-function correlation, a set of the clickable PD-L1 inhibitors bearing varied OEG spacer lengths was screened to determine the optimal molecular configuration for PD-L1 degradation on the surface of cell membrane (Fig. 2A). The outperformed D5B with the longest OEG spacer displayed a $EC_{50}$ value of 5.4 μM in wild-type 4T1 breast tumor cells and a $EC_{50}$ value of 6.2 μM in wild-type B16-F10 melanoma tumor cells in vitro, which were 21.5- and 16.7-fold lower than that of the parental molecular BMS-1, respectively (table S1). Above findings indicated the advantage of covalent binding of the inhibitor for highly efficient PD-L1 degradation by stably conjugating the clickable inhibitor on the surface of tumor cells (Fig. 2E).

PD-L1 degradation study in vivo demonstrated that free D5B marginally reduced PD-L1 abundance in the tumor tissue in vivo due to lack of tumor-specificity and insufficient tumor distribution of the small-molecule inhibitor. In contrast, D5B delivered with the $pH_e$-activatable PCP nanoparticles displayed 26.3-fold higher tumor concentration than the free D5B when examined at 24 hours after intravenous administration. This markedly increased intratumor distribution of the clickable inhibitor resulted in fivefold higher PD-L1 degradation efficacy than the free D5B group in vivo (Fig. 5, E and F), verifying the advantage of tumor-targeted delivery of the clickable inhibitor for spatially confined PD-L1 inhibition. It was worth noting that, despite that the $pH_i$-activatable (PDP@D5B) and pH-insensitive nanoparticles (PBP@D5B) delivered comparable D5B to the tumor site, they did not affect PD-L1 abundance in the tumor tissue (Fig. 5J), highlighting the crucial importance of spatial delivery of the clickable PD-L1 inhibitor into the tumor extracellular microenvironment for PD-L1 inhibition in vivo. Furthermore, achieving precise tumor therapy by combining PD-L1 degradation and RT, the D5B-loaded $pH_e$-activatable nanoparticles were readily incorporated with Gd-chelated PPa as a NIRFI and MRI tracer, which enabled NIRFI and MRI-guided radioimmunotherapy of solid tumors. The clickable PD-L1 inhibitor boosted RT by inhibiting RT-induced PD-L1 up-regulation on the surface of both tumor cells and M2-type TAMs and thereby regressed both the primary and abscopal tumors and prevented lung metastasis of the breast tumor (Figs. 6R and 7O).

In summary, we reported a $pH_e$-activatable nanoplatform for tumor-specific delivery of the clickable PD-L1 inhibitor and spatially confined degradation of PD-L1 in vitro and in vivo. The clickable PD-L1 inhibitor can covalently bind with PD-L1 on the surface of tumor cells and TAM membrane via bioorthogonal click chemistry and metabolic glycan engineering, thereby enabling local enrichment of the PD-L1 inhibitor and highly efficient PD-L1 degradation. The outperformed D5B inhibitor with the optimized OEG spacer displayed over 20-fold higher PD-L1 degradation efficacy than the parental BMS-1 molecule, validating the unique advantage of the covalent binding strategy. Biodistribution study in vivo further demonstrated that the $pH_e$-responsive markedly elongated the blood circulation and increased tumor accumulation of the clickable inhibitor in vivo, which allowed tumor-specific PD-L1 degradation without affecting PD-L1 abundance in the normal tissues. The D5B-loaded $pH_e$-responsive PCP@D5B nanoparticles elicited antitumor immune response for inhibiting 4T1 breast and B16-F10 melanoma tumor growth in vivo. The PCP@D5B nanoparticles integrating NIRFI and MRI tracers performed dual imaging-guided precise RT of breast and melanoma tumors to minimizing the reverse effects of RT. Combinatory radioimmunotherapy with the PCPGd@D5B nanoparticles and RT efficiently mitigated RT stress-induced ITM by reducing PD-L1 abundance on the surface of both tumor cells and TAM membrane, resulting in marked eradication of 4T1 breast and B16-F10 melanoma tumors in 50% of the tumor-bearing mice. Combinatory therapy of PCPGd@D5B nanoparticles and RT induced systemic immunological memory to inhibit the abscopal tumor growth and prevent lung metastasis of the 4T1 breast tumor. The clickable inhibitor–based radioimmunotherapy (e.g., PCPGd@D5B + RT) demonstrated improved antitumor performance than the conventional radioimmunotherapy (e.g., αPD-L1 + RT) due to tumor-specific PD-L1 degradation with the clickable inhibitor. Overall, tumor-specific PD-L1 degradation with the clickable PD-L1 inhibitor might represent a generalizable strategy for potentiating cancer

immunotherapy. One concern for the clickable PD-L1 inhibitor could be azide labeling of tumor cells, which is highly dependent on intratumoral injection of $Ac_4ManAz$, which remains to be optimized for labeling deep seated and metastatic tumors. A robust strategy is highly desirable to specifically incorporate azide group into PD-L1 glycoproteins of the most lethal tumor types including pancreatic cancer and glioblastoma, aiming to promote clinical translation of the clickable PD-L1 inhibitors.

## MATERIALS AND METHODS

### Materials

1-(3-Dimethylaminopropyl)-3-ethylcarbodiimide hydrochloride, 4-dimethylaminopyridine,triethylamine,*N*,*N*-diisopropylethylamine, 1-hydroxybenzotriazole, *N*,*N*-dimethylacetamide (anhydrous), dimethyl sulfoxide (DMSO; anhydrous), *N*,*N*-dimethylformamide (anhydrous), and 2,2′-azobis (2-methylpropionitrile) were all purchased from J&K Chemical (Shanghai, China). 4-Cyano-4-(dodecylsulfanylthiocarbonyl) sulfanylpentanoic acid, $mPEG_{113}$-$NH_2$, ethylene glycol, triethylene glycol, pentaethylene glycol, 2-hydroxyethyl methacrylate, butyl methacrylate, 2-(diisopropyl amino) ethyl methacrylate, D-mannosaminehydrochloride,2-azidoaceticacid,*N*-hydroxysuccinimide, acetic anhydride, and pyridine were all purchased from were all purchasedfromSigma-Aldrich(Shanghai,China).2-(Hexamethyleneimino) ethyl methacrylate (C7A) was prepared according to the method described previously (*38*). PPa was purchased from Debai Biotechnology Co. Ltd. (Shanghai, China). 2-Hydroxyethyl methacrylate was purchased from TCI (Shanghai, China). BMS-1, 4′,6-diamidino-2-phenylindole (DAPI), and formaldehyde were all purchased from Dalian Meilun Biotech Co. Ltd. (Dalian, China). DBCO-carboxylic acid and DBCO-amine were purchased from Click Chemistry Tools (Shanghai, China). FITC-labeled wheat germ agglutinin and LysoTracker Green were obtained from Life Technologies (Shanghai, China). Other reagents and solvents were obtained from Sinopharm Co. Ltd. (Shanghai, China).

### Cell lines

Tumor cell lines of 4T1 murine breast cancer, B16-F10 murine melanoma cancer, MBA-MD-231 human breast cancer, HN30 human head and neck cancer, Panc02 murine pancreatic cancer, CT26 and MC38 murine colorectal cancer, and A549 human non–small cell lung cancer were obtained from the cell bank of Chinese Academy of Sciences (Shanghai, China). The cells were cultured in complete Dulbecco's modified eagle medium cell culture medium containing 10% fetal bovine serum, glucose (2.5 g/liter), sodium pyruvate (0.11 g/liter), penicillin G sodium (100 U/ml), and streptomycin sulfate (100 μg/ml). Cells were maintained at 37°C in a 5.0% $CO_2$ atmosphere.

### Animals

BALB/c and C57BL/6 mice (female, 6 to 8 weeks old, 18 to 20 g) were obtained from the Shanghai Experimental Animal Center (Shanghai, China). All animal procedures were carried out under the guidelines approved by the Institutional Animal Care and Use Committee (IACUC) of the Shanghai Institute of Material Medica, Chinese Academy of Sciences (IACUC number 2023-10-YHJ-09 and 2023-10-YHJ-10).

### Preparation of the acid-insensitive PBP@D5B nanoparticles

Briefly, 50 μl of PBP (10 mg/ml in DMSO) and 10 μl of D5B (5 mg/ml in DMSO) were mixed and added to 1 ml of deionized water under ultrasound. The organic solvent was removed by dialysis tube [molecular weight cut off (MWCO) of 3.5 kDa). The PBP@D5B suspension was then concentrated to 500 μl via ultrafiltration.

### Preparation of $pH_e$-responsive PCP@D5B nanoparticles

PCP (50 μl; 10 mg/ml in DMSO) and D5B (10 μl; 5 mg/mL in DMSO) via vortex were added to 1 ml of deionized water under ultrasound. The organic solvent was removed by dialysis tube (MWCO of 3.5 kDa). The PCP@D5B was then concentrated via ultrafiltration to 500 μl.

### Preparation of $pH_i$-activatable PDP@D5B nanoparticles

The mixture of 50 μl of PDP (10 mg/ml in DMSO) and 10 μl of D5B (5 mg/ml in DMSO) via vortex was added to 1 ml of deionized water under ultrasound. The organic solvent was removed by dialysis tube (MWCO of 3.5 kDa). The PDP@D5B nanoparticle suspension was then concentrated via ultrafiltration to 500 μl. The hydrodynamic diameter of above nanoparticles was measured by DLS using the Zetasizer. The morphology of various nanoparticles was observed by TEM.

### Acid-triggered drug release in vitro

Briefly, PBP@D5B, PCP@D5B, and PDP@D5B nanoparticles (1.0 ml, 5.0 mg/ml) in a dialysis tube (MWCO of 3.5 kDa) were, respectively, immersed in 10 ml of release medium [PBS buffer (pH 7.4 and 6.5) with 0.5% Tween 80] at 37°C. To monitor the release of D5B, 10 μl of PBP@D5B, PCP@D5B, and PDP@D5B were collected via ultrafiltration at predetermined times, and the remaining sample was immersed in the release medium again. Then, the quantification of the D5B release was conducted using high-performance liquid chromatography.

### Acid-triggered dissociation and fluorescence activation of the PBP@D5B, PCP@D5B, and PDP@D5B

Briefly, PBP@D5B, PCP@D5B, or PDP@D5B nanoparticles (100 μl, 0.5 mg/ml) were dispersed in 1.0 ml of PBS buffer at pH 7.4, 7.0, 6.8, 6.6, 6.4, or 6.2. Then, the fluorescence spectrum of PPa was measured using fluorescence spectroscopy (excitation of 615 nm and emission of 680 nm), the fluorescence image was collected using an IVIS imaging system, and the morphology of dissociation was detected using TEM.

### Biodistribution of the PBP@D5B, PCP@D5B, and PDP@D5B nanoparticles in vivo

Briefly, 4T1 tumor model was established by subcutaneously injecting $1 \times 10^6$ of 4T1 cells into the right flank mammary of mice. The tumor volume reached ~100 $mm^3$ at 10 days after inoculation. The PBP@D5B, PCP@D5B, and PDP@D5B nanoparticles were intravenously injected into the tumor-bearing mice at an identical PPa dose of 2.0 mg/kg and D5B dose of 2.0 mg/kg. The mice were anesthetized at the predetermined time points, and the fluorescence imaging was recorded using an IVIS imaging system (PerkinElmer).

### Acid-triggered MRI activation of the PCPGd@D5B nanoparticles in vitro and in vivo

Briefly, PCPGd@D5B nanoparticles were dispersed in PBS buffer at pH 7.4, 7.0, 6.8, 6.6, 6.4, or 6.2; the concentration of PCPGd@D5B was 0, 62.5, 125, 250, 500 and 1000 μg/ml; the concentration of $Gd^{3+}$ was 0, 0.016, 0.033, 0.065, 0.130, and 0.261. Then, $T_1$-weighted MR images and $T_1$ map of PCPGd@D5B in a 96-well plate containing 100 μl of aliquots of PCPGd@D5B suspension were measured using 9.4-T BioSpin MRI (Bruker, Germany).

To perform MRI in vivo, a 4T1 tumor model was established by subcutaneously injecting $1 \times 10^6$ of 4T1 cells on the flank of Balb/c mouse. The mice were intravenously injected with 100 μl of PCP-Gd@D5B nanoparticle at an identical $Gd^{3+}$ dose of 1.5 mg/kg when the tumor volume reached ~100 $mm^3$. The MRI of the 4T1 tumor was imaged at predetermined intervals.

### Azide labeling of tumor cells in vitro

4T1 cells were cultured in six-well plates at a density of 150,000 cells per well incubating with 25 μM $Ac_4$ManAz in cell culture medium for 3 days. After washing with PBS, the cells were collected via centrifuge and incubated with 10 μM DBCO-FITC or FITC for 1.0 hours at 4°C. The cells were then analyzed by flow cytometry and CLSM.

### IFN-γ–up-regulated PD-L1 on the surface of tumor cell membrane

Briefly, 4T1 or B16-F10 cells were cultured in six-well plates at 50,000 cells per well and incubated with IFN-γ (12.5 ng/ml) for 24 hours. The cells were then collected for Western blot measurement and stained by BMS-1–PPa for flow cytometry measurement, with anti–PD-L1–phycoerythrin (PE) staining as positive control. Generally, 4T1 cells were cultured in 24-well plates at a density of 10,000 cells per well and subjected to the same treatment method, and, then, the cells were stained by DAPI for CLSM measurement.

### $pH_e$-triggered click reaction and PD-L1 inhibition in vitro

4T1 cells were cultured in six-well plates at a density of 50,000 cells in each well incubating with 25 μM $Ac_4$ManAz in culture medium for 3 days. Then, the cells were collected to incubate with PBP@DBCO-FITC, PCP@ DBCO-FITC, and PDP@ DBCO-FITC (containing 1.0 μM DBCO-FITC) pretreated with PBS buffer (pH 7.4 and 6.5) for 1.0 hours at 4°C. After washing with cold PBS, the FITC fluorescent signal on cells was detected using flow cytometry. Generally, the 4T1 cells were cultured in 24-well plates at a density of 10,000 cells in each well treated with the same method and then stained by DAPI for CLSM measurement.

For PD-L1 inhibition study, 4T1 cells were cultured in six-well plates at a density of 50,000 cells per well and incubated with 25 μM $Ac_4$ManAz and IFN-γ (12.5 ng/ml) for 3 days. Then, the cells were collected to incubate with PBP@D5B, PCP@D5B, and PDP@D5B (containing with 10 μM D5B) pretreated with PBS buffer (pH 7.4 and 6.5) for 24 hours at 37°C. After washing with cold PBS, the cells were collected and stained with anti–PD-L1–PE for flow cytometry. Meanwhile, 4T1 cells were cultured in 24-well plates at a density of 10,000 cells in each well treated with the same method and then stained with DAPI and anti–PD-L1–FITC for CLSM measurement.

### The clickable PD-L1 inhibitor enhanced PD-L1 degradation of wild-type tumor cells

For PD-L1 degradation with the clickable PD-L1 inhibitor, 4T1 or B16-F10 tumor cells were cultured in six-well plates at a density of 50,000 cells per well and incubated with 25 μM $Ac_4$ManAz for 3 days. The cells were then incubated with BMS-1, D1B, D3B, and D5B (concentration of 1.25, 2.5, 5.0, and 10.0, at equal doses of BMS-1) for 24 hours. Then, the cell membrane was collected for Western blot analysis, while the tumor cells were gathered for flow cytometry measurement. The PD-L1 inhibition rate was calculated by using the formula:

*Inhibition rate* % = $(MFI_{PBS}\text{-}MFI_{treatment})/ MFI_{PBS}$ (*MFI*, median fluorescence intensity).

### The clickable PD-L1 inhibitor downregulated IFN-γ–induced PD-L1 in tumor cells in vitro

For enhancement of PD-L1 inhibition through the covalent strategy, 4T1 or B16-F10 cells were cultured in six-well plates at a density of 50,000 cells in each well incubating with 25 μM $Ac_4$ManAz and IFN-γ (12.5 ng/ml) in culture medium for 3 days. Then, the cells were incubated with BMS-1, D1B, D3B, or D5B for 48 hours at equal doses of 0, 1.25, 2.5, and 5.0 μM BMS-1. Then, the cell membrane was extracted for Western blot analysis and the cells were collected for flow cytometry measurement.

### Antitumor performance of the clickable PD-L1 inhibitor in vivo

To evaluate the antitumor performance of the covalent strategy, the xenograft 4T1 and B16-F10 tumor model was established. Briefly, female BALB/c or C57BL/6 mice (6 to 8 weeks) were subcutaneously injected with $1 \times 10^6$ 4T1 or B16-F10 cells in the left flank. The tumor-bearing mice were randomly divided into different groups when the tumor volume reached 50 $mm^3$. Thereafter, the mice were treated with different formulations in 100 μL of PBS every 3 days for three times. 4T1 tumor-bearing mice were randomly divided into different groups, (G1) $Ac_4$ManAz + PBS, (G2) $Ac_4$ManAz + D5B, (G3) $Ac_4$ManAz + PBP@D5B, (G4) $Ac_4$ManAz + PDP@D5B, and (G5) $Ac_4$ManAz + PCP@D5B. The B16-F10 tumor-bearing mice were randomly divided into different groups: (G1) $Ac_4$ManAz + PBS, (G2) $Ac_4$ManAz + PCP@D5B, and (G3) $Ac_4$ManAz + aPD-L1. $Ac_4$ManAz (20 mg/kg) was intratumorally injected once daily for 3 days (days 1, 2, and 3). D5B, PBP@D5B, PDP@D5B, and PCP@D5B (containing with 5 mg/kg in BMS-1 equivalent) were intravenously injected, or αPD-L1 (10 mg/kg) was intraperitoneally injected on day 4. The tumor volume was calculated by using the formula: $V = L \times W \times W/2$ ($L$, the longest dimension; and $W$, the shortest dimension).

### Antitumor performance of the clickable PD-L1 inhibitor and RT in vivo

To evaluate antitumor efficacy, the 4T1 or B16-F10 tumor models were established by subcutaneously injecting $1 \times 10^6$ 4T1 or B16-F10 cells on the flank of female BALB/c or C57BL/6 mice (6 to 8 weeks). The tumor-bearing mice were randomly divided into different groups when the tumor volume reached 50 $mm^3$. Thereafter, the mice were treated with different formulations in 100 μl of sterile PBS every 3 days for three times. The 4T1 or B16-F10 tumor-bearing mice were randomly divided into different groups: (G1) $Ac_4$ManAz + PBS, (G2) $Ac_4$ManAz + PCPGd@D5B, (G3) $Ac_4$ManAz + PCPGd+RT, and (G4) $Ac_4$ManAz + PCPGd@D5B + RT. $Ac_4$ManAz (20 mg/kg) was intratumorally injected once daily for 3 days (days 1, 2, and 3). D5B, PCPGd@D5B (containing with 5 mg/kg in BMS-1 equivalent) were intravenously injected on day 4. The dose of RT is 6 Gy.

### Biosafety evaluation of the clickable PD-L1 inhibitor in vivo

The major organs (e.g., heart, liver, lung, spleen, and kidneys) were harvested 14 days after treatment with different formulations, fixed in 4% formalin solution, dehydrated, and subjected to hematoxylin and eosin staining.

### Evaluation of antitumor immunity in vivo

To evaluate the mechanism of antitumor immunity of clickable PD-L1 inhibitor alone treatment or in combination with RT treatment in vivo, DC maturation and intratumoral infiltration of CTLs were detected

using flow cytometry. Briefly, 4T1 or B16-F10 tumor models were established in BALB/c or C57BL/6 mice as described above. When the tumor volume reached 150 $mm^3$, the mice received treatments as described above. The mice were euthanized 3 days after treatment, and TDLNs were collected to obtain the single-cell suspension, and, then, the cells were stained with anti–CD11c-FITC, anti–CD86–allophycocyanin (APC), and anti–CD80-PE antibodies to evaluate DC maturation. The tumors were harvested at 5 days after three cycles of treatments cut into small pieces and immersed in a solution of hyaluronidase (1 mg/ml), collagenase IV (1 mg/ml), and deoxyribonuclease I (0.2 mg/ml) for 45 min at 37°C. After filtration through a 70-μm filter to obtain the single-cell suspension, the cells were stained with anti–CD45-PE, anti–CD3-PercpCy5.5, anti–CD8-APC, and anti–CD4-FITC to analyze intratumoral infiltration of T lymphocytes; the cells were stained with anti–CD45-FITC, anti–CD3-Cy5.5, anti–CD8-APC, and anti–IFN-γ–FITC to analyze the tumor-infiltrating $CD8^+IFN\text{-}\gamma^+$ T lymphocytes; and the cells were stained with anti–CD45-FITC, anti–CD11b-PercpCy5.5, anti–CD206-PE, and anti–CD86-APC to analyze TAMs. The cells were stained with anti–CD45-FITC, anti–CD11b-PercpCy5.5, and anti–PD-L1–PE for analyzing PD-L1 of tumor cells and TAMs. All antibodies were used at a dilution of 1:200. All the cells were stained with the antibodies for 30 min at 4°C. To stain intracellular proteins, the cell suspension was fixed and permeabilized with the commercial buffer Flow Cytometry Permeabilization/Wash Buffer I (R&D Systems), followed by intracellular staining with anti–IFN-γ–FITC.

To examine IFN-γ secretion in tumors, 4T1 tumor-bearing mice were treated with the nanoparticles when the tumor volume reached 150 $mm^3$. The tumors were collected and homogenized at 1, 3, and 7 days after treatment. The tumors were digested and centrifuged to obtain the supernatant. IFN-γ in the supernatants was measured using an ELISA kit according to the protocol.

To evaluate the antitumor immunity of combinatory therapy with the clickable PD-L1 inhibitor and RT in vivo, tumor-infiltrating CTLs and TAMs were detected using immunofluorescence staining of the tumor sections. Briefly, 4T1 or B16-F10 tumors were established in BALB/c or C57BL/6 mice as described above. The mice received treatments as described above when the tumor volume reached 150 $mm^3$. The mice were euthanized 3 days after treatment, and the tumors were collected for immunofluorescence staining. The tumors were embedded in paraffin, frozen sectioned, and stained with antibodies against PD-L1, TAM, and CD8 for CLSM examination. $PD\text{-}L1^+$ cells, TAMs, and $CD8^+$ T cells in tumor sections were semiquantitatively analyzed using ImageJ software.

### Statistical analysis

Statistical analysis was performed using GraphPad Prism 9.1. Data are presented as means ± SD.

## Supplementary Materials

**This PDF file includes:**

Supplementary Methods
Tables S1 and S2
Figs. S1 to S20

## REFERENCES AND NOTES


1. D. S. Chen, I. Mellman, Oncology meets immunology: The cancer-immunity cycle. *Immunity* **39**, 1–10 (2013).
2. L. P. Andrews, H. Yano, D. A. A. Vignali, Inhibitory receptors and ligands beyond PD-1, PD-L1 and CTLA-4: Breakthroughs or backups. *Nat. Immunol.* **20**, 1425–1434 (2019).
3. P. Sharma, J. P. Allison, The future of immune checkpoint therapy. *Science* **348**, 56–61 (2015).
4. A. V. R. Kornepati, R. K. Vadlamudi, T. Curie, Programmed cell death 1 ligand 1 signals in cancer cells. *Nat. Rev. Cancer* **22**, 174–189 (2022).
5. D. B. Doroshow, S. Bhalla, M. B. Beasley, L. M. Sholl, K. M. Kerr, S. Gnjatic, I. I. Wistuba, D. L. Rimm, M. S. Tsao, F. R. Hirsch, PD-L1 as a biomarker of response to immune-checkpoint inhibitors. *Nat. Rev. Clin. Oncol.* **18**, 345–362 (2021).
6. P. Sharma, J. P. Allison, Dissecting the mechanisms of immune checkpoint therapy. *Nat. Rev. Immunol.* **20**, 75–76 (2020).
7. P. Sharma, J. P. Allison, Immune checkpoint therapy: Forging ahead. *Sci. Transl. Med.* **14**, eadf2947 (2022).
8. C. Sun, R. Mezzadra, T. N. Schumacher, Regulation and function of the PD-L1 checkpoint. *Immunity* **48**, 434–452 (2018).
9. J. D. Wolchok, V. Chiarion-Sileni, R. Gonzalez, J. J. Grob, P. Rutkowski, C. D. Lao, C. L. Cowey, D. Schadendorf, J. Wagstaff, R. Dummer, P. F. Ferrucci, M. Smylie, M. O. Butler, A. Hill, I. Marquez-Rodas, J. B. A. G. Haanen, M. Guidoboni, M. Maio, P. Schoffski, M. S. Carlino, C. Lebbe, G. McArthur, P. A. Ascierto, G. A. Daniels, G. V. Long, T. Bas, C. Ritchings, J. Larkin, F. S. Hodi, Long-term outcomes with nivolumab plus ipilimumab or nivolumab alone versus ipilimumab in patients with advanced melanoma. *J. Clin. Oncol.* **40**, 127–137 (2022).
10. A. Almutairi, N. Alsaid, J. Martin, H. M. Babiker, A. McBride, I. Abraham, Comparative efficacy and safety of immunotherapies targeting PD-1/PD-L1 pathway for previously treated advanced non-small cell lung cancer: Bayesian network meta-analysis. *Crit. Rev. Oncol. Hematol.* **142**, 16–25 (2018).
11. G. Morad, B. A. Helmink, P. Sharma, J. A. Wargo, Hallmarks of response, resistance, and toxicity to immune checkpoint blockade. *Cell* **184**, 5309–5337 (2021).
12. Q. Li, Q. Chen, P. C. Klauser, M. Y. Li, F. Zheng, N. X. Wang, X. Li, Q. Zhang, X. Fu, Q. Wang, Y. Xu, L. Wang, Developing covalent protein drugs via proximity-enabled reactive therapeutics. *Cell* **182**, 85–97.e16 (2020).
13. J. Singh, R. C. Petter, T. A. Baillie, A. Whitty, The resurgence of covalent drugs. *Nat. Rev. Drug Discov.* **10**, 307–317 (2011).
14. A. Abdeldayem, Y. S. Raouf, S. N. Constantinescu, R. Moriggl, P. T. Gunning, Advances in covalent kinase inhibitors. *Chem. Soc. Rev.* **49**, 2617–2687 (2020).
15. H. Wang, D. J. Mooney, Metabolic glycan labelling for cancer-targeted therapy. *Nat. Chem.* **12**, 1102–1114 (2020).
16. P. V. Chang, J. A. Prescher, E. M. Sletten, J. M. Baskin, I. A. Miller, N. J. Agard, A. Lo, C. R. Bertozzi, Copper-free click chemistry in living animals. *Proc. Natl. Acad. Sci. U.S.A.* **107**, 1821–1826 (2010).
17. J. A. Prescher, D. H. Dube, C. R. Bertozzi, Chemical remodeling of cell surfaces in living animals. *Nature* **430**, 873–877 (2004).
18. B. Hou, L. Zhou, H. Wang, M. Saeed, D. Wang, Z. Xu, Y. Li, H. Yu, Engineering stimuli-activatable Boolean logic prodrug nanoparticles for combination cancer immunotherapy. *Adv. Mater.* **32**, e1907210 (2020).
19. J. Du, L. A. Lane, S. Nie, Stimuli-responsive nanoparticles for targeting the tumor microenvironment. *J. Control. Release* **219**, 205–214 (2015).
20. S. Li, Y. Zhang, S.-H. Ho, B. Li, M. Wang, X. Deng, N. Yang, G. Liu, Z. Lu, J. Xu, Q. Shi, J.-Y. Han, L. Zhang, Y. Wu, Y. Zhao, G. Nie, Combination of tumour-infarction therapy and chemotherapy via the co-delivery of doxorubicin and thrombin encapsulated in tumour-targeted nanoparticles. *Nat. Biomed. Eng.* **4**, 732–742 (2020).
21. B. A. Webb, M. Chimenti, M. P. Jacobson, D. L. Barber, Dysregulated pH: A perfect storm for cancer progression. *Nat. Rev. Cancer* **11**, 671–677 (2011).
22. Y. Wang, K. Zhou, G. Huang, C. Hensley, X. Huang, X. Ma, T. Zhao, B. D. Sumer, R. J. DeBerardinis, J. M. Gao, A nanoparticle-based strategy for the imaging of a broad range of tumors by nonlinear amplification of microenvironment signals. *Nat. Mater.* **13**, 204–212 (2014).
23. H.-H. Lee, Y.-N. Wang, W. Xia, C.-H. Chen, K.-M. Rau, L. Ye, Y. Wei, C.-K. Chou, S.-C. Wang, M. Yan, C.-Y. Tu, T.-C. Hsia, S.-F. Chiang, K. S. C. Chao, I. I. Wistuba, J. L. Hsu, G. N. Hortobagyi, M.-C. Hung, Removal of N-Linked glycosylation enhances PD-L1 detection and predicts anti-PD-1/PD-L1 therapeutic efficacy. *Cancer Cell* **36**, 168–178.e4 (2019).
24. Y.-N. Wang, H.-H. Lee, J. L. Hsu, D. Yu, M.-C. Hung, The impact of PD-L1 N-linked glycosylation on cancer therapy and clinical diagnosis. *J. Biomed. Sci.* **27**, 77 (2020).
25. Q. Zhu, H. Wang, S. Chai, L. Xu, B. Lin, W. Yi, L. Wu, O-GlcNAcylation promotes tumor immune evasion by inhibiting PD-L1 lysosomal degradation. *Proc. Natl. Acad. Sci. U.S.A.* **120**, e2216796120 (2023).
26. L. Rastelli, S. Rajagopal, C. Gajendran, N. M. Sadhu, Z. Mohd, R. Gosu, D. Friedmann-Morvinski, S. Kandan, S. Birudukota, S. Srinivasan, V. Krishnakumar, S. Wahid, A. Siddiqui, S. Viswakarma, A. Narayan, G. Rudresh, S. R. Mullurwar, D. Sher, S. Mansur, D. Sivanandhan, Novel, small molecule inhibitors of PD-1/PD-L1 pathway. *J. Clin. Oncol.* **40**, 2597–2597 (2022).

27. P. Russomanno, G. Assoni, J. Amato, V. M. D'Amore, R. Scaglia, D. Brancaccio, M. Pedrini, G. Polcaro, V. La Pietra, P. Orlando, M. Falzoni, L. Cerofolini, S. Giuntini, M. Fragai, B. Pagano, G. Donati, E. Novellino, C. Quintavalle, G. Condorelli, F. Sabbatino, P. Seneci, D. Arosio, S. Pepe, L. Marinelli, Interfering with the tumor-immune interface: Making way for triazine-based small molecules as novel PD-L1 inhibitors. *J. Med. Chem.* **64**, 16020–16045 (2021).
28. H. K. Koblish, L. X. Wu, L.-C. S. Wang, P. C. C. Liu, R. Wynn, J. Rios-Doria, S. Spitz, H. Liu, A. Volgina, N. Zolotarjova, K. Kapilashrami, E. Behshad, M. Covington, Y.-O. Yang, J. W. Li, S. Diamond, M. Soloviev, K. O'Hayer, S. Rubin, C. Kanellopoulou, G. J. Yang, M. Rupar, D. DiMatteo, L. Lin, C. Stevens, Y. Zhang, P. Thekkat, R. Geschwindt, C. Marando, S. Yeleswaram, J. Jackson, P. Scherle, R. Huber, W. Yao, G. Hollis, Characterization of INCB086550: A potent and novel small-molecule PD-L1 inhibitor. *Cancer Discov.* **12**, 1482–1499 (2022).
29. G. Chen, A. C. Huang, W. Zhang, G. Zhang, M. Wu, W. Xu, Z. Yu, J. Yang, B. Wang, H. Sun, H. Xia, Q. Man, W. Zhong, L. F. Antelo, B. Wu, X. Xiong, X. Liu, L. Guan, T. Li, S. Liu, R. Yang, Y. Lu, L. Dong, S. McGettigan, R. Somasundaram, R. Radhakrishnan, G. Mills, Y. Lu, J. Kim, Y. H. Chen, H. Dong, Y. Zhao, G. C. Karakousis, T. C. Mitchell, L. M. Schuchter, M. Herlyn, E. J. Wherry, X. W. Xu, W. Guo, Exosomal PD-L1 contributes to immunosuppression and is associated with anti-PD-1 response. *Nature* **560**, 382–386 (2018).
30. J. Ye, B. Hou, F. Chen, S. Zhang, M. Xiong, T. Li, Y. Xu, Z. Xu, H. Yu, Bispecific prodrug nanoparticles circumventing multiple immune resistance mechanisms for promoting cancer immunotherapy. *Acta. Pharm. Sin. B* **12**, 2695–2709 (2022).
31. Z. Zhou, H. He, K. Wang, X. Shi, Y. Wang, Y. Su, Y. Wang, D. Li, W. Liu, Y. Zhang, L. Shen, W. Han, L. Shen, J. J. Ding, F. Shao, Granzyme A from cytotoxic lymphocytes cleaves GSDMB to trigger pyroptosis in target cells. *Science* **368**, eaaz7548 (2020).
32. D. H. Kaplan, V. Shankaran, A. S. Dighe, E. Stockert, M. Aguet, L. J. Old, R. D. Schreiber, Demonstration of an interferon gamma-dependent tumor surveillance system in immunocompetent mice. *Proc. Natl. Acad. Sci. U.S.A.* **95**, 7556–7561 (1998).
33. C. S. Garris, S. P. Arlauckas, R. H. Kohler, M. P. Trefny, S. Garren, C. Piot, C. Engblom, C. Pfirschke, M. Siwicki, J. Gungabeesoon, G. J. Freeman, S. E. Warren, S. Ong, E. Browning, C. G. Twitty, R. H. Pierce, M. H. Le, A. P. Algazi, A. I. Daud, S. I. Pai, A. Zippelius, R. Weissleder, M. J. Pittet, Successful anti-PD-1 cancer immunotherapy requires T cell-dendritic cell crosstalk involving the cytokines IFN-γ and IL-12. *Immunity* **49**, 1148–1161.e7 (2018).
34. J. Guo, Y. Liang, D. Xue, J. Shen, Y. Cai, J. Zhu, Y.-X. Fu, H. Peng, Tumor-conditional IL-15 pro-cytokine reactivates anti-tumor immunity with limited toxicity. *Cell Res.* **31**, 1190–1198 (2021).
35. F. Chen, T. Li, H. Zhang, M. Saeed, X. Liu, L. Huang, X. Wang, J. Gao, B. Hou, Y. Lai, C. Ding, Z. Xu, Z. Xie, M. Luo, H. Yu, Acid-ionizable iron nanoadjuvant augments STING activation for personalized vaccination immunotherapy of Cancer. *Adv. Mater.* **35**, e2209910 (2023).
36. A. H. Sharpe, E. J. Wherry, R. Ahmed, G. J. Freeman, The function of programmed cell death 1 and its ligands in regulating autoimmunity and infection. *Nat. Immunol.* **8**, 239–245 (2007).
37. J. Naidoo, D. B. Page, B. T. Li, L. C. Connell, K. Schindler, M. E. Lacouture, M. A. Postow, J. D. Wolchok, Toxicities of the anti-PD-1 and anti-PD-L1 immune checkpoint antibodies. *Ann. Oncol.* **26**, 2375–2391 (2015).
38. B. Hou, J. Ye, J. Li, Z. Xu, H. Yu, In-situ clickable prodrug nanoplatform locally activates T lymphocytes to potentiate cancer immunotherapy. *Nano Today* **47**, 101661 (2022).
39. M. Zhou, J. Wang, J. Pan, H. Wang, L. J. Huang, B. Hou, Y. Lai, F. Wang, Q. Guan, F. Wang, Z. Xu, H. Yu, Nanovesicles loaded with a TGF-β receptor 1 inhibitor overcome immune resistance to potentiate cancer immunotherapy. *Nat. Commun.* **14**, 3593 (2023).
40. J. Ye, B. Hou, S. Madiha, Z. Xu, H. Yu, Engineered nanomedicine mitigates resistance of cancer immunotherapy. *Acc. Mater. Res.* **7**, 697–708 (2022).
41. F. Zhou, J. Ga, Y. Tan, Z. Zou, S. Jiao, Z. Zhou, H. Xu, Z. Xu, H. Yu, Z. Xu, Engineering chameleon prodrug nanovesicles to increase antigen presentation and inhibit PD-L1 expression for circumventing immune resistance of Cancer. *Adv. Mater.* **34**, 2102668 (2021).
42. E. B. Golden, A. Chhabra, A. Chachoua, S. Adams, M. Donach, M. Fenton-Kerimian, K. Friedman, F. Ponzo, J. S. Babb, J. Goldberg, S. Demaria, S. C. Formenti, Local radiotherapy and granulocyte-macrophage colony-stimulating factor to generate abscopal responses in patients with metastatic solid tumors: A proof-of-principle trial. *Lancet Oncol.* **16**, 795–803 (2015).
43. B. Hou, L. Yi, D. Hu, Z. Luo, D. Gao, C. Li, B. Xing, J.-W. Wang, C. N. Lee, R. Zhang, Z. Sheng, B. Zhou, X. Liu, A swallowable X-ray dosimeter for the real-time monitoring of radiotherapy. *Nat. Biomed. Eng.* **7**, 1242–1251 (2023).
44. X. Chen, J. Song, X. Chen, H. Yang, X-ray-activated nanosystems for theranostic applications. *Chem. Soc. Rev.* **48**, 3073–3101 (2019).
45. C. Twyman-Saint Victor, A. J. Rech, A. Maity, R. Rengan, K. E. Pauken, E. Stelekati, J. L. Benci, B. H. Xu, H. Dada, P. M. Odorizzi, R. S. Herati, K. D. Mansfield, D. Patsch, R. K. Amaravadi, L. M. Schuchter, H. Ishwaran, R. Mick, D. A. Pryma, X. Xu, M. D. Feldman, T. C. Gangadhar, S. M. Hahn, E. J. Wherry, R. H. Vonderheide, A. J. Minn, Radiation and dual checkpoint blockade activate non-redundant immune mechanisms in cancer. *Nature* **520**, 373–377 (2015).
46. Z. S. Morris, E. I. Guy, D. M. Francis, M. M. Gressett, L. R. Werner, L. L. Carmichael, R. K. Yang, E. A. Armstrong, S. Huang, F. Navid, S. D. Gillies, A. Korman, J. A. Hank, A. L. Rakhmilevich, P. M. Harari, P. M. Sondel, In situ tumor vaccination by combining local radiation and tumor-specific antibody or immunocytokine treatments. *Cancer Res.* **76**, 3929–3941 (2016).
47. H. E. Barker, J. T. E. Paget, A. A. Khan, K. J. Harrington, The tumour microenvironment after radiotherapy: Mechanisms of resistance and recurrence. *Nat. Rev. Cancer* **15**, 409–425 (2015).
48. Y. Zhang, R. N. Sriramaneni, P. A. Clark, J. C. Jagodinsky, M. Ye, W. Jin, Y. Wang, A. Bates, C. P. Kerr, T. Le, R. Allawi, X. Wang, R. Xie, T. C. Havighurst, I. Chakravarty, A. L. Rakhmilevich, K. A. O'Leary, L. A. Schuler, P. M. Sondel, K. Kim, S. Q. Gong, Z. S. Morris, Multifunctional nanoparticle potentiates the in-situ vaccination effect of radiation therapy and enhances response to immune checkpoint blockade. *Nat. Commun.* **13**, 4948 (2022).
49. S. R. Gordon, R. L. Maute, B. W. Dulken, G. Hutter, B. M. George, M. N. Mccracken, R. Gupta, J. M. Tsai, R. Sinha, D. Corey, A. M. Ring, A. J. Connolly, I. L. Weissman, PD-1 expression by tumour-associated macrophages inhibits phagocytosis and tumour immunity. *Nature* **545**, 495–499 (2017).
50. C. Wan, Y. Sun, Y. Tian, L. Lu, X. Dai, J. Meng, J. Huang, Q. He, B. Wu, Z. Zhang, K. Jiang, D. Hu, G. Wu, J. F. Lovell, H. Jin, K. Yang, Irradiated tumor cell-derived microparticles mediate tumor eradication via cell killing and immune reprogramming. *Sci. Adv.* **6**, eaay9789 (2020).
51. L. Cassetta, J. W. Pollard, A timeline of tumor-associated macrophage biology. *Nat. Rev. Cancer* **23**, 238–257 (2023).
52. R. Offringa, L. Kotzner, B. Huck, K. Urbahns, The expanding role for small molecules in immuno-oncology. *Nat. Rev. Drug Discov.* **21**, 821–840 (2022).
53. M. Konstantinidou, T. Zarganes-Tzitzikas, K. Magiera-Mularz, T. A. Holak, A. Domling, Immune checkpoint PD-1/PD-L1: Is there life beyond antibodies? *Angew. Chem. Int. Ed.* **57**, 4840–4848 (2018).


**Acknowledgments:** We thank the Mass Spectrometry System and the cell sorter BD Influx of the National Facility for Protein Science in Shanghai (NFPS), Shanghai Advanced Research Institute, CAS. **Funding:** This work was supported by the National Natural Science Foundation of China (22074043 and 32311530041 to Z.X. and U22A20328 to H.Y.); Science and Technology Commission of Shanghai Municipality (23ZR1475000 and 20430711800 to H.Y. and 23490712700 to Z.X.); the State Key Laboratory of Chemical Biology, Shandong Postdoctoral Science Foundation (SDCX-ZG-202400071 to B.H.); Shanghai Post-doctoral Excellence Program (2023696 to B.H.); China Postdoctoral Science Foundation (2023M743657 to B.H.); and Postdoctoral Fellowship Program of CPSF (GZC20232844 to B.H.). **Author contributions:** Writing—original draft: B.H., W.C., W.H., and Z.X. Conceptualization: B.H., J.G., Z.X., and H.Y. Investigation: B.H. and Z.X. Writing—review and editing: B.H., W.H., and Z.X. Methodology: B.H., J.Y., L.H., F.C., H.Z., J.P., Y.L., J.G., Y.Z., Z.X., and H.Y. Resources: B.H., H.Z., J.G., Y.Z., and Z.X. Funding acquisition: B.H. and Z.X. Data curation: B.H., H.Z., W.H., and Z.X. Validation: B.H., H.Z., J.G., and Z.X. Form analysis: B.H. Supervision: W.H. and Z.X. Project administration: B.H. and Z.X. Visualization: B.H., J.Y., L.H., J.G., W.H., and Z.X. **Competing interests:** The authors declare that they have no competing interests. **Data and materials availability:** All data needed to evaluate the conclusions in the paper are present in the paper and/or the Supplementary Materials.

Submitted 11 May 2024
Accepted 15 October 2024
Published 15 November 2024
10.1126/sciadv.adq3940